

# **Belle II silicon vertex detector tests and studies for efficient searches of new physics**

---

**James Webb**  
538230

A thesis presented for the degree of  
Master of Science

Faculty of Physics  
Melbourne University



THE UNIVERSITY OF  

---

MELBOURNE

*Supervisor: Professor Geoffrey Taylor*

# 1 Abstract

The Belle II experiment is designed with the aim of collecting high luminosity data with an integrated luminosity of  $50 \text{ ab}^{-1}$  for searching for phenomena beyond the standard model. The high luminosity environment requires that the SVD2 present from the Belle experiment be replaced to handle the expected increase in occupancy and durability to radiation. Belle II SVD is designed with both of these requirements in mind. The electrical qualification assessment is one of the most important procedures in the production of the Belle II SVD. Detecting and classifying the electrical defects present within the detectors. The full EQA process involves both electrical measurements of during the assembly of the detector, aswell as successful readout following charge creation within the detector through laser pulse injection.

A study of improvements for the reconstruction of  $D^*$  decay through  $dE/dx$  measurement of the daughter slow pion is also undertaken. Searching for additional information in tracks curling through the SVD for improved resolution in the  $dE/dx$  measurement for the purpose of improved particle identification.

## **2 Statement of originality**

Chapter 4 and 5 are an original review of the literature performed by the author.

Chapter 6 contains the work performed by the author in EQA and laser procedure.

Chapter 7 contains research performed by the author in design and improvement of the laser scan system.

Chapter 8 contains research performed by the author in looking for improvements in  $dE/dx$  measurement for low momentum decays.

All work is original and created by the author unless otherwise stated.

# Contents

<b>1</b>	<b>Abstract</b>	<b>1</b>
<b>2</b>	<b>Statement of originality</b>	<b>2</b>
<b>3</b>	<b>Introduction</b>	<b>4</b>
<b>4</b>	<b>The Belle II Detector</b>	<b>4</b>
4.1	Silicon Vertex Detector . . . . .	5
<b>5</b>	<b>Semiconductor tracking</b>	<b>8</b>
5.1	Charge transport . . . . .	8
5.2	Induced Charge - Ramo's Theorem . . . . .	10
5.3	Particle Identification using $dE/dx$ . . . . .	10
<b>6</b>	<b>Layer 3 SVD electrical quality assessment</b>	<b>13</b>
6.1	Data acquisition . . . . .	13
6.2	Electrical Results . . . . .	15
6.3	Laser test . . . . .	19
6.4	Laser Results . . . . .	21
<b>7</b>	<b>Silicon Clustering</b>	<b>23</b>
7.1	Internal reflections from laser signal . . . . .	23
7.2	Angular laser injection . . . . .	26
7.3	Cosmic muon calibration sample . . . . .	28
<b>8</b>	<b>Low momentum tracking improvements using <math>dE/dx</math></b>	<b>31</b>
8.1	$D^*$ data sample . . . . .	31
8.2	Belle II simulation . . . . .	32
8.3	$dE/dx$ from trackfit parameters . . . . .	32
8.4	Curling tracks in the SVD . . . . .	33
<b>9</b>	<b>Conclusion</b>	<b>36</b>
<b>A</b>	<b>Laser optics</b>	<b>37</b>
<b>B</b>	<b>Polyimide IR absorption</b>	<b>38</b>
<b>C</b>	<b>Helical coordinate system</b>	<b>38</b>
<b>D</b>	<b>Additional ladder electrical and laser results</b>	<b>39</b>
D.1	L3.903 . . . . .	39
D.2	L3.002 . . . . .	40
<b>E</b>	<b>Electrical Test Procedure</b>	<b>42</b>

### 3 Introduction

The Belle experiment at the KEKB collider located at KEK(Tsukuba, Japan) was built to measure many decay modes branching ratios to test for the standard model (SM), as well as the mixing induced CP violation in  $B^0$  system predicted by Kobayashi and Maskawa [1]. Over a decade of operation, numerous results arising from measurements taken by the Belle detector, have confirmed with good precision the theoretical predictions of the standard model. The successful theory of CP violation led to Kobayashi and Maskawa being awarded the Nobel prize in 2008 [2].

One of the best processes for observing CP violates comes from decay of neutral B mesons. B mesons are bound states of a light u or d quark and a heavy b quark. The B mesons can be produced in large quantities at so called *B factories*, asymmetric electron-positron colliders operated at the  $\Upsilon(4S)$  resonance. At 10.58 GeV the  $\Upsilon(4S)$  is only slightly heavier than twice the mass of  $B^0$  or  $B^\pm$ . Because of this, the  $\Upsilon(4S)$ , consisting of a  $b\bar{b}$  quark pair, will decay into mostly  $B^0\bar{B}^0$  and  $B^+B^-$  pairs. Due to the asymmetric beam energies, the B mesons produced in the  $\Upsilon(4S)$  decay are not at rest with respect to the lab frame, but are boosted in the forward direction. By reconstructing the decay vertices, accurate measurement of decay times for each B meson can be made, which is integral for many measurements of CP violation.

The KEKB collider currently holds the world record for instantaneous luminosity at  $2.1 \times 10^{34} \text{cm}^2 \text{s}^{-1}$ , more than twice the designed luminosity and a total integrated luminosity of  $1 \text{ab}^{-1}$ . [3]. The successor to KEKB, SuperKEKB should be able to reach a total integrated luminosity of twice KEKB soon after operation begins and is designed to reach an ultimate luminosity of  $8 \times 10^{35} \text{cm}^2 \text{s}^{-1}$  and total integrated luminosity of  $50 \text{ab}^{-1}$  over a six year run period, 40 times the peak instantaneous luminosity value of the previous KEKB collider.

Due to the nature of having a much higher luminosity, many of the components of the Belle detector will need to be replaced and new detectors added. The Belle II detector will need to be able to cope with much higher background levels, key consideration towards data readout and radiation tolerance of the innermost electronics is necessary.

The aim of SuperKEKB a *super flavour factory*, is to gather high-statistics datasets for high precision measurements that allow for the search of significant deviations from the standard model predictions for rare decay modes. Although B decay results are in good agreement with the SM and confirm CKM structure for quark mixing and CP violation, some measurements show tension with SM predictions. Much larger datasets are necessary to investigate whether these tensions are hits for new physics. One such example of a rare SM process in which possible contributions of NP may be large enough to observe is the  $B \rightarrow K\pi$  decay mode [4].

### 4 The Belle II Detector

The SuperKEKB accelerator aims to produce an instantaneous luminosity of  $8 \times 10^{35} \text{cm}^2 \text{s}^{-1}$  and total integrated luminosity of  $50 \text{ab}^{-1}$  by the year 2020. The luminosity is given by

$$\mathcal{L} = \frac{\gamma_{\pm}}{2er_e} \left( 1 + \frac{\sigma_y^*}{\sigma_x^*} \right) \frac{I_{\pm} \xi_{y,\pm}}{\beta_{y,\pm}^*} \frac{R_L}{R_{\xi y}} \quad (1)$$

Where  $\gamma$  is the Lorentz factor,  $r_e$  is the classical electron radius,  $\sigma_y^*/\sigma_x^*$  is the beam size aspect ratio,  $I$  is the beam current,  $\beta_y^*$  is the vertical beta function at the interaction point,  $\xi_y$  is the beam-beam parameter, and  $R_L/R_{\xi y}$  is a geometrical factor. The  $\pm$  subscript refers to the quantity that is associated with the low energy positron (-) and high energy electron beams (+).

In order for SuperKEKB to reach a luminosity 40 times that of KEKB several improvements had to be added. The main increase to the luminosity comes from the significant reduction in beam size at the collision point (nano beam scheme). The beta functions are reduced in the x direction from 1200mm to 32/25mm for the high energy electron/low energy positron respectively. The beta functions are also reduced in the y direction from 5.9mm to 0.27/0.42 mm. The beta function reduction is a result of changing the interaction region using new focusing quadrupole magnets. Furthermore the designed instantaneous luminosity of  $8 \times 10^{35} \text{ cm}^{-2} \text{ s}^{-1}$  and total integrated luminosity of  $50 \text{ ab}^{-1}$  requires a reduction in the beam energy asymmetry from 3.6/8 GeV to 4/7 GeV and an enlargement in the crossing angle from 22 mrad to 83 mrad. Due to the increase in luminosity higher background levels will be present compared to KEKB. The main source of background arising from Touschek scattering [3].

## 4.1 Silicon Vertex Detector

The Belle Silicon Vertex Detector (SVD2) was previously equipped with four layers of double sided silicon detectors (DSSDs) read out by the VA1TA front-end chip with a nominal shaping time of 800ns. The KEKB accelerator delivers a quasi-continuous beam, operating at an RF of approximately 509MHz. The majority of the SVD2 hits in the innermost layers are not related to the triggered events, but rather off-time background due to the large sensitive time window of the VA1TA readout, about  $2 \mu\text{s}$ . Over the lifetime of the KEKB accelerator the luminosity steadily grew up to  $2.1 \times 10^{34} \text{ cm}^{-2} \text{ s}^{-1}$ . When it was shutdown in 2010, the innermost layer of the SVD2 were facing an average occupancy of 10%. An occupancy at this level or above leads to degradation in hit efficiency and resolution due to the merging of clusters which lead to incorrect track association. For the transition to SuperKEKB the SVD2 was no longer viable and a redesign with a focus on occupancy reduction was necessary.

The Belle II SVD consists of four layers of double-sided silicon sensors centred around the beampipe at radii of  $r = 38/80/115/140 \text{ mm}$ . The increase in radial position compared to its predecessor, Belle SVD2, is due to room needed to fit the pixel layers at  $r = 14/22 \text{ mm}$  [5]. The arrangement of the SVD layers as shown in figure 1, covers a polar angle range from  $17^\circ$  to  $150^\circ$ . This asymmetry corresponds with the forward boost arising from the asymmetrically colliding electron and positron beams. To improve the performance of the SVD in the forward region, a slant angle was applied to the outer three layers to increase the spatial resolution, while minimising the number of sensors required. Each of the layers are comprised of double sided silicon sensors, of varied sizes, made from 6" silicon wafers. The double sided detectors have a nominal thickness of  $300 \mu\text{m}$  and are comprised of separate N and P-type bulk substrate with N and P side aluminium electrodes on the top and bottom running at  $90^\circ$  to each other.

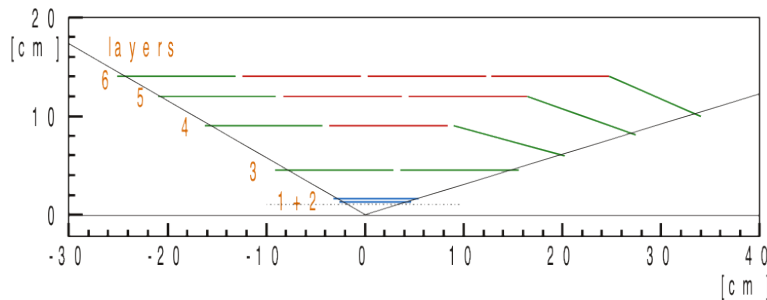


Figure 1: Side on view of the SVD ladder geometry. Each of the four SVD layers are shown along with the two pixel layers (grey). Each of the three different sensor sizes and shapes, along with the pitch are labelled in the legend. The given dimensions of the sensors refer to the active areas. Taken from [5]

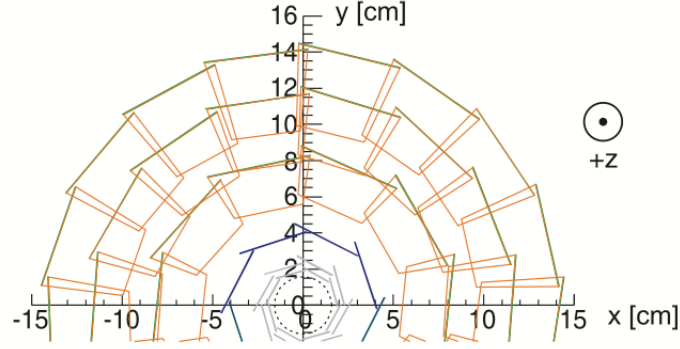


Figure 2: Cross-section view of the SVD ladder geometry. Taken from [5]

The silicon strip readout of the SVD will be performed by the APV25 (Analogue Pipeline Voltage,  $0.25\mu\text{m}$ ) chip[6]. The APV25 chip is the first readout chip for a high energy physics experiment to be constructed from  $0.25\mu\text{m}$  CMOS technology. Originally developed for the CMS silicon tracker at the LHC, the APV25 readout chip satisfies the requirements for the Belle II SVD, eg. low shaping time, high radiation tolerance.

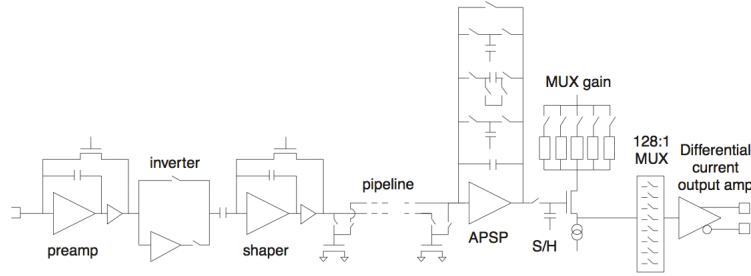


Figure 3: Building block diagram of one of the 128 channels of the APV25 front-end readout chip design [6]

The APV25 chip consists of 128 identical channels, each made up of the components shown in figure 3. Each APV25 channel consists of a low-noise preamplifier coupled to a shaping amplifier to produce a CR-RC pulse shape with nominal peaking time of 50 ns. The CR-RC pulse shape is sampled at a nominal clock rate of 40 MHz (in Belle II it will operate at 31.8MHz, 1/16 of the SuperKEKB RF) into a 192-cell deep analogue pipeline (ring buffer) with an index FIFO (First In First Out) which can label up to 32 cells for readout following a received trigger. The marked cells are not overwritten until the stored data has been output by the chip. Following the pipeline is the analogue pulse shape processor (APSP). This is a switched capacitor filter that is able to perform *deconvolution*. For the CMS experiment the APV25 operates with the clock rate set to 40MHz to coincide with the bunch crossing frequency of the LHC. The phase can be adjusted such that only the peak of the shaping will be sampled whilst operating in *peak mode*. The APV25 can use three consecutive samples around the peak of the shaping curve to perform a deconvolution with its internal APSP circuit. This operation reverses the shaping function, allowing for the readout samples corresponding to the bunch crossing to be identified without ambiguity.

Operation of deconvolution mode requires that the clock frequency be 40 MHz and clock synchronous particle signals to properly adjust the phase. As SuperKEKB will operate with a quasi-continuous beam, the deconvolution feature is not able to be used. In this case the APSP circuit will simply pass on the pipeline contents. The strip data is finally multiplexed through three hierarchical stages and sent to the differential-current-mode output.

Due to the fast shaping time, the noise of the APV25 is higher than that of amplifiers with a long shaping time. As a result the input capacitance of the amplifier must be minimised in order to maintain a reasonable signal-to-noise ratio. Therefore it is necessary that the chips be positioned as closely as possible to the sensor. It is this limitation that lead to the "Origami" chip on sensor design for layers 4,5,6 [6].

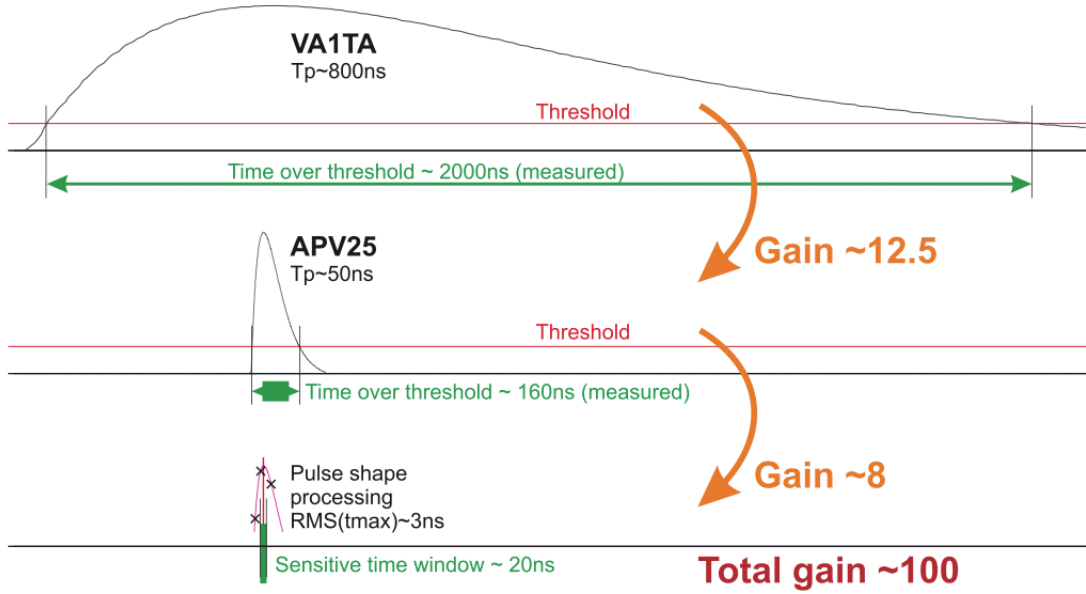


Figure 4: Comparison of shaping time between the VA1TA, APV25 single peak, and APV25 multi-peak mode. Estimated reduction in occupancy is shown. Taken from [6]

The replacement of VA1TA readout chips (800ns shaping time) with APV25 (50ns shaping time) for the Belle II SVD will reduce the sensitive time window and thus the occupancy significantly. Depending factors such as the noise thresholds and shaper output waveform, the reduction may not be exactly a factor of 16. In both cases it is necessary to consider the time over threshold, which was found to be 2000 ns and 160 ns respectively, yielding an improvement of factor 12.5. [6].

Depending upon the estimated background in the Belle II SVD, this factor of 12.5 improvement in the occupancy should be sufficient in meeting the sub-10% occupancy requirement in the innermost layers. Expected occupancy in the innermost layers for the Belle II SVD working in the SuperKEKB are estimated to be 6.7%, but with large uncertainties as the Belle II background conditions are not yet known [6]. To deal with higher than expected occupancy, the multi-peak mode of the APV25 can be employed to reduce the sensitive time window. Multi-peak mode takes three consecutive samples along the shaped waveform to be used in off-detector reconstruction of the peaking time and along with precise trigger timing, allow for off-time background hits to be discarded. Measurements with prototype modules have



shown that the RMS timing precision is of the order of a few nanoseconds [6], thus the sensitive time window can be set to approximately 20ns. This allows for the occupancy of the innermost layers to be reduced by up to a factor of 100 compared to the VATA based SVD2 modules within Belle.

The SVD is enclosed around a gas filled chamber called the central drift chamber (CDC). Charged particles traversing the CDC ionising the gas and generate ions which are accelerated by the electric field and collected by the wires throughout the chamber.

## 5 Semiconductor tracking

Semiconductor detectors are used in nuclear and particle physics for the observation of transit of charged particles. Precise information such as cluster position, timing and charge deposited in the sensor is fundamental to the reconstruction of charged particle tracks, as well as particle identification. The most significant interaction when it comes to the SVD is the ionisation of atoms. This process describes the creation of electron-hole pairs in the silicon detector.

### 5.1 Charge transport

The purpose of the SVD is to be able to measure the trajectories of charged particles. This is fundamental to the reconstruction of decay vertices. When a charged particle crosses the sensor energy is lost, ionising surrounding matter and creating electron-hole pairs which drift under the effect of bias voltage.

In silicon detectors there are two distinct ways in which motion of charge carriers are distinguished: drift and diffusion. The drift of particles in the silicon caused by an external electric field only affects the free charged particles in the semiconductor lattice. While diffusion is not limited to any specific particle, including crystal imperfections and impurities.

When in thermal equilibrium the average thermal energy of a conduction electron can be obtained from the equipartition energy  $1/2 k_B T$  units of energy per degree of freedom. The electrons in the semiconductor are free to move in three dimensional space, so they have three degrees of freedom. From this the kinetic energy of these electrons is given by  $\frac{1}{2} m^* \nu_{th}^2 = \frac{3}{2} k_B T$ , where  $m^*$  is the effective mass of the electrons (which takes into account the influence of crystal lattices) and  $\nu_{th}$  is the average thermal velocity. The thermal motion of individual electrons can be visualised as a series of random scattering from collisions with impurity atoms, lattice atoms and other scattering centres. The random motion of the electron results in a net displacement of zero over a sufficiently large time period. When a small electric field is applied each electron in the silicon will feel a force  $\vec{F} = -q \vec{E}$  and will be accelerated in the opposite direction to the electric field during the time inbetween collisions. The electric field provides an additional velocity component to the thermal motions of the electrons, called the drift velocity. The drift velocity may be calculated by equating the momentum applied to the electron between two collisions  $\vec{p}_{drift} = -q \vec{E} \tau$  and the momentum gained  $\vec{p}_{drift} = m^* \vec{\nu}_{drift}$  where  $m^*$  is the effective mass and  $\tau$  is the mean free time between scattering collisions [7].

$$-q \vec{E} \tau = m^* \nu_{drift} \quad (2)$$

$$\nu_{drift,e} = - \left( \frac{q\tau}{m^*} \right) \vec{E} \quad (3)$$

$$= -\mu_e \vec{E} \quad (4)$$

Where the proportionality factor  $\mu_e$  is called the electron mobility with units of  $cm^2/Vs$ . A similar expression can be found in the same way for holes in the valence band:  $\nu_{drift,h} = \mu_h \vec{E}$ . The negative sign is removed in this result as the holes drift in the same direction as the electric field.

From the above equation it is implied that a charge carrier can be accelerated as fast as one desires by increasing the electric field. However, this is not the case. Under a high electric field, the free charge carriers gain energy from the field. The mobility  $\mu(E)$  decreases with increasing electric field until it saturates, a parameterisation for the solution is given in [8]

$$\mu_d = \frac{\mu_0}{\left(1 + \left(\frac{\mu_0 E}{\nu_s}\right)^\beta\right)^{\frac{1}{\beta}}} \quad (5)$$

where  $\mu_0$  is the low field mobility,  $\nu_s$  the saturation velocity and the additional parameter  $\beta$ . Each of these quantities are found empirically and are temperature dependent.

Charge carriers may also be transported by diffusion. If there exists a spatial variation of carrier concentration in the semiconductor material, the carriers tend to move from a region of high concentration to one of low concentration. The carrier flow gives rise to a current  $J_n = -qF = qD_n \frac{dn}{dx}$ , working in one dimension. Using the equipartition of energy in this one dimensional case gives the relationship  $J_n = qD_n \frac{dn}{dx} = q \left( \frac{kT}{q} \mu_n \right) \frac{dn}{dx}$ . Which leads us to the Einstein relation

$$D_n = \left( \frac{kT}{q} \mu_n \right) \quad (6)$$

The Einstein relation relates diffusivity and mobility that characterise the carrier transport by diffusion and drift in a semiconductor. The relation similarly applies to hole mobility.

When a magnetic field is introduced, a Lorentz force acts upon the motion of the charge carriers perpendicular to their motion, and the magnetic field itself. This force creates a so-called Lorentz angle between the direction of the electric field, and the motion of the charge carriers.  $\vec{F}_L = -q\vec{v} \times \vec{B} = -qv_z B_y$

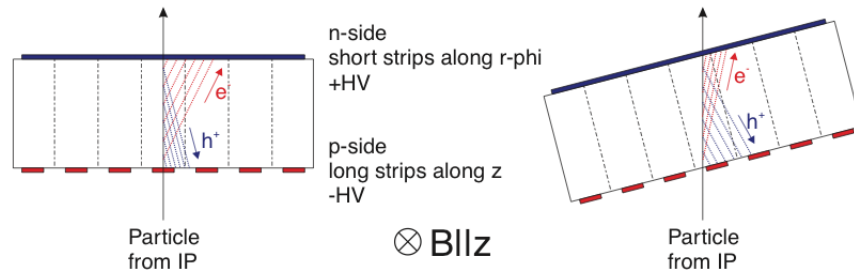


Figure 5: Charge carrier drift shown with applied magnetic field. On the left charge carriers are deflected by the Lorentz force. On the right it is shown that the overall spread of charge can be minimised by tilting the sensor to reduce electron deflection. Taken from [6]

The force gives the carriers a new velocity,  $v_L$ , where the angle between the initial and final direction is  $\tan(\theta_L) = \frac{v_x}{v_z}$ .

$$\tan(\theta_L) = \frac{v_x}{v_z} = \frac{\Delta x}{d} = \mu_H B = r_H \mu B \quad (7)$$

Where  $d$  corresponds to the drift distance along the electric field and  $\Delta x$  the shift in signal position (distance between signal entry and electrode detecting the cluster).  $\mu_H$  is the Hall mobility, drift mobility in a magnetic field. The drift mobility without the presence of a magnetic field is related to the Hall mobility by  $r_H = \frac{\mu_H}{\mu}$ . This factor describes the mean free time between carrier collisions, which are dependent on the carrier energy.

## 5.2 Induced Charge - Ramo's Theorem

A moving charge in the presence of a grounded electrode will induce an instantaneous electric current on the electrode. For multiple electrodes within the vicinity of the moving charge carriers, each will have some induced electric current dependent upon the electric field from the moving charge carriers. The total induced charge on an electrode once all of the charges have arrived at the electrodes is equal to the actual arrived charge at the electrode.

The theorem devised by Ramo in 1939 introduced novel way to calculate the induced charge at each point on the grounded electrode configuration. The theorem states that the instantaneous induced current on a given electrode is given by

$$i_k = q\vec{v} \cdot \vec{F}_k \quad (8)$$

where  $v$  is the velocity of the charge carrier,  $q$  is the charge of the carrier and  $F$  is the weighting field. The weighting field is determined by applying a unit potential to the electrode considered and zero potential to all other electrodes in the system. The weighting field depends only upon the geometry of the electrodes and determines how the motion of charge couples to a given electrode [9].

## 5.3 Particle Identification using $dE/dx$

Charged particles traversing the silicon semiconductor will interact with the surrounding matter creating electron-hole pairs via ionisation. The total number of electron-hole pairs are related to the total energy loss of the particle. This process has a heavy dependence upon the momentum of the incident particles, which define the maximum kinetic energy that can be transferred to the electrons in the medium.

The maximum energy transferred in a single collision for a particle of mass  $M$  is given by

$$W_{max} = \frac{2m_e c^2 \beta^2 \gamma^2}{1 + 2\gamma m_e/M + (m_e/M)^2} \quad (9)$$

In the low energy limit  $2\gamma m_e/M \ll 1$  the energy transfer function can be approximated as [10]

$$W_{max} = 2m_e c^2 \beta^2 \gamma^2 \quad (10)$$

The expression for maximum energy transfer is dependent upon  $\beta\gamma$ , not the particles mass.

The mean energy loss for relativistic charged particles in the region  $0.1 < \beta\gamma < 1000$  is described by the Bethe-Bloch equation,

$$\left\langle -\frac{dE}{dx} \right\rangle = K z^2 \frac{Z}{A} \frac{1}{\beta^2} \left[ \frac{1}{2} \ln \frac{2m_e c^2 \beta^2 \gamma^2 W_{max}}{I^2} - \beta^2 - \frac{\delta(\beta\gamma)}{2} \right] \quad (11)$$

Where  $K$  is a constant defined by  $4\pi N_A r_e^2 m_e c^2$ ,  $z$  is the charge number of incident particle,  $Z$  is the atomic number of absorbing particle,  $A$  is atomic mass of absorbing particle,  $M$  incident particle mass,  $W_{max}$  is the maximum energy transfer in a single collision (in MeV),  $I$  the mean excitation potential (in eV),  $\delta(\beta\gamma)$  the density effect correction to ionisation energy loss.

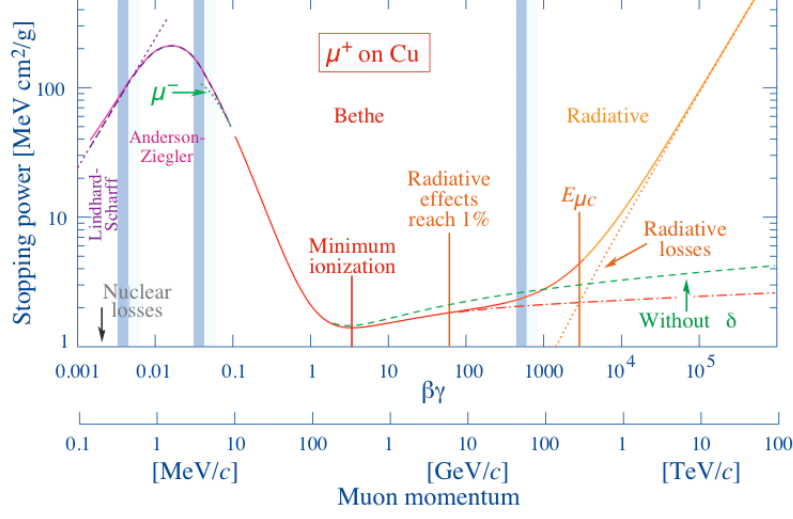


Figure 6: Stopping power  $\langle -dE/dx \rangle$  as a function of  $\beta\gamma = \frac{p}{m_{\mu}c}$  for positive muons traversing copper. The solid curves indicate the total energy loss, dashed curves signifying different components. The vertical lines separate the different approximations for the energy loss model. Taken from [10]

The Bethe-Bloch stopping power function for muons in copper is shown in 6. It can be seen that a peak in ionisation exists for low  $\beta\gamma$  which falls off for increasing particle momenta. Particles in this region will fail to reach the surrounding detector, or be absorbed by the beam pipe. Due to this only particles in the downward slope ( $\frac{1}{\beta^2}$  region) will be measured. At  $\beta\gamma \approx 5$ , a minimum in the mean energy loss is reached - particles which fall in this region are hence known as minimally ionising particles (MIP's). For  $\beta\gamma$  larger than the MIP, the energy loss once again increases, leading to the logarithmically increasing relative rise.

The function  $\delta(\beta\gamma)$  describes the aptly named density effect correction which takes into account the suppression of the relativistic rise. As the incident particles energy increases, their transverse electric field flattens and extends. The media becomes polarized, limiting the field extension and effectively suppressing this part of the logarithmic rise. This effect is largely dependent upon the density of the medium's material. As a result of this, the probability of interaction is significantly reduced for particles with high momentum, the energy deposited in the medium approaching a constant value, the Fermi plateau [10]. This effect is quite pronounced in solids where the relativistic rise is almost entirely hidden.

The Bethe-Bloch equation describes the momentum dependence of the mean energy loss. For each momentum value the energy loss forms a distribution around this mean value. This distribution characterises the energy lost to the electrons of the medium through ionisation.

The distribution of secondary electrons ( $\delta$  rays) with kinetic energy  $T \gg I$  is

$$\frac{d^2 N}{dT dx} = \frac{1}{2} K z^2 \frac{Z}{A} \frac{1}{\beta^2} \frac{F(T)}{T^2} \quad (12)$$

Where  $\beta$  is the velocity of the incident particle,  $F$  is a spin-dependent factor, for spin-0 particles  $F(T) = (1 - \beta^2 T/W_{max})$  form factors for spin-1/2, spin-1 particles are given in [11]. For  $T \ll W_{max}$   $F(T)$  is approximately unity. It can be seen from the above equation that  $\delta$  rays of high energy are relatively uncommon.

In 1944 Lev Landau theorised a description for these process and the resultant energy loss distribution. For detectors of moderate thickness, the energy loss probability distribution is described by the asymmetric Landau distribution. The long tail corresponding to the high energy transfers created by  $\delta$  rays.

$$\Delta_p = \xi \left[ \ln \frac{2mc^2 \beta^2 \gamma^2}{I} + \ln \frac{\xi}{I} + j - \beta^2 - \delta(\beta\gamma) \right] \quad (13)$$

where  $\xi = (K/2)\langle Z/A \rangle (x/\beta^2)$  in MeV for a detector of thickness  $x$ , in  $gcm^{-2}$ ,  $j = 0.2$  [12].

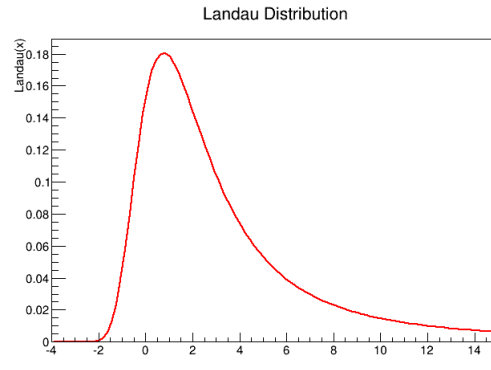


Figure 7: Plot of a normalised Landau distribution

As a result of the skewed nature of the Landau distribution statistical quantities of interest, mean, variance, are divergent and ultimately undefined.

## 6 Layer 3 SVD electrical quality assessment

The Belle II SVD construction is being undertaken by collaborators from five institutes situated across the globe. Layer 3 being constructed by Melbourne, layer 4 TIFR (Mumbai), Layer 5 HEPHY (Vienna), Layer 6 IMPU (Tokyo) and forward/backward sub-assemblies PISA. Throughout the production of the Silicon Vertex Detector ladders, electrical characterisation studies are performed at key stages to confirm the functionality of readout electronics and semiconductor sensor alike. Early detection of defective components, or improper assembly allow for the possibility of correction, or damage mitigation for the ladder under construction.



Figure 8: Completed ladder with N side facing up

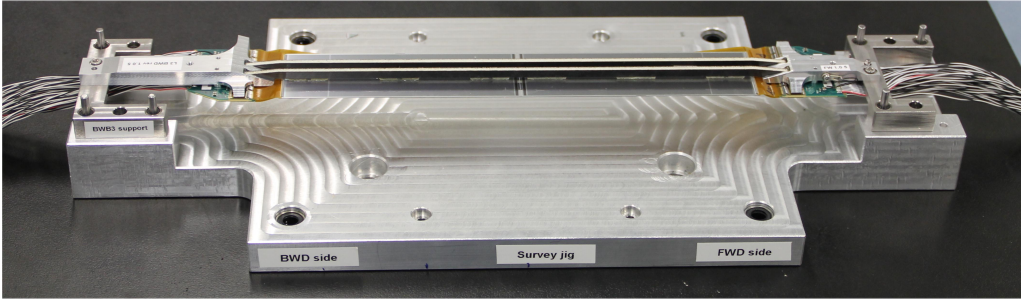


Figure 9: Completed ladder with P side facing up

A completed layer 3 ladder consists of two halves denoted as forward and backward sub-assemblies. Each half consists of a DSSD attached to a double sided hybrid

### 6.1 Data acquisition

Electronic readout of the APV25 is performed on-site using the APVDAQ (Analogue Pipeline 0.25 $\mu$ m Data Acquisition) system developed by High Energy PHYSics (HEPHY) [13]. The APVDAQ readout system allows the analog differential current signal from the APV25 chip to read out at full clock frequency 40 MHz. Each APVDAQ VME module is able to readout up to four APV25 chips, scaling up to four APVDAQ VME provides to required readout capabilities for testing the Layer 3 DSSDs. Additionally the readout system has full support for all operation modes capable by the APV25 chip [14].

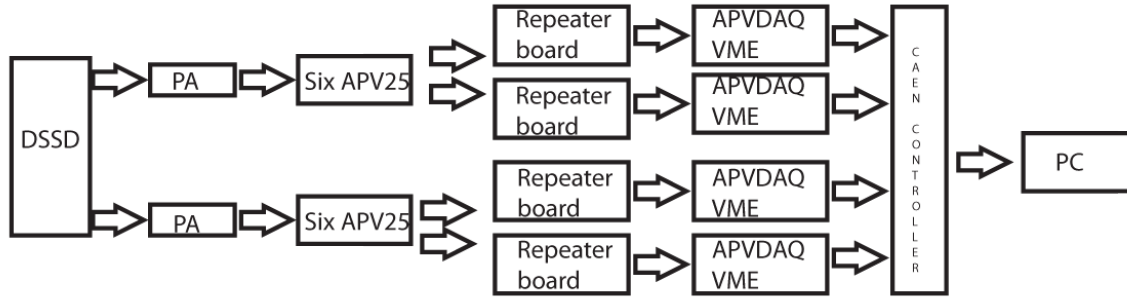


Figure 10: Readout chain for the SVD

The electrical testing setup entails four APVDAQ VME modules along with a CAEN VME controller card to interface to the ADC readout. A single APVDAQ module distributes the clock and trigger information to the additional slave modules. Each of the APVDAQ boards are then connected to an AC repeater board which acts as a local interface between the APV25 hybrid and the remote VME boards, repeating signals between the two devices. Additionally the repeater boards contain an isolated connection to the bias line on the hybrid board, allowing for the DSSD to be provided with high voltage. A further benefit of the repeater board is the ability to draw from the floating voltage received by the repeater boards in order to increase the voltage supplied to the APV25 chip, allowing for the cancellation of additional current flowing into the chip as a result of a pinhole.

Following the ADC (Analogue to Digital Converter) readout performed by the APVDAQ for each individual APV25 chip, an ADC count sample is recorded for each channel. The first 600 samples read out by the APVDAQ are used to establish the pedestal and noise present in each channel that data is being drawn. The process of this is as follows:

- The Pedestal (PED) is defined as the average baseline ADC from 300 randomly triggered ADC samples for each channel.
- The Raw Noise is defined as RMS of the fluctuation in ADC with respect to the pedestal for each channel.
- The Common Mode Correction is defined as the correction applied to reduce the effect of the common mode shift (CMS) - the electronic noise can be classed into two categories, intrinsic and external noise. The intrinsic noise is due to the leakage current and parasitic capacitance of the detector, which varies with channel. External noise affects the entire chip and is generated by an external source. The effect of the external noise will be a shift of all channels in a constant direction.

$$PED[i][j] = \frac{1}{300} \sum_{n=0}^{299} RawADC[n][i][j] \quad (14)$$

$$Rawnoise[i][j] = \sqrt{\frac{1}{300} \sum_{n=300}^{599} (RawADC[n][i][j] - PED[i][j])^2} \quad (15)$$

$$CMS[n][i] = \frac{1}{32} \sum_{j=0}^{31} (rawADC[n][i][j] - PED[i][j]) \quad (16)$$

$$Signal[n][i][j] = RawADC[n][i][j] - PED[i][j] - CMS[n][i] \quad (17)$$

$$Noise[i][j] = \sqrt{\frac{1}{300} \sum_{n=300}^{599} (RawADC[n][i][j] - PED[i][j] - CMS[n][i])^2} \quad (18)$$

Where  $n$  is the event number,  $i$  is the APV number and  $j$  is the channel number.

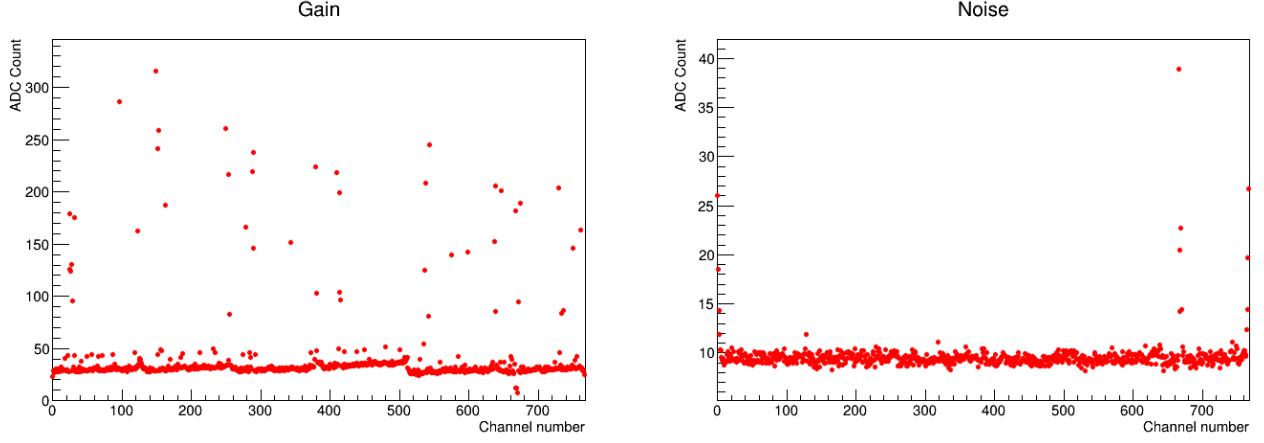
Each APV25 contains an internal calibration circuit for the purpose of easily testing the functionality of the CR-RC shaping amplifier without the need for any external equipment. This allows for the amplifier, a key component of the readout to be tested periodically over the lifetime of the experiment for both functionality and calibration. The calibration circuit is used to apply a voltage step pulse to a series of capacitors which are connected to the amplifier. The injected charge is given by  $Q=CV$ . The calibration consists of an on-chip pulse generator injecting a charge equal to 1 MIP passing through  $320 \mu\text{m}$  of silicon  $\approx 24,000 e^-$  into each channel in groups of 16. Fine resolution pulse shape mapping is obtained through delayed trigger requests with respect to the charge injection. The timing of the pulse injections can be adjusted in steps of  $1/8$  of the clock,  $3.125\text{ns}$  @  $40\text{MHz}$  [15].

## 6.2 Electrical Results

The electrical readout from the APV25 provides vital information in regards to the quality of the assembled module and as such the aforementioned electrical testing (noise, calibration,  $V_{sep}$ ) is performed several times throughout the production of each SVD ladder.

At any point in the production of the SVD ladders, an electrical test may be performed, provided the APV25 channels have been wire-bonded to the silicon wafer via aluminium bond pads on each strip. Undertaking electrical testing prior to applying a bias voltage to the semiconductor will result in large noise in the signal readout. Charge carriers are free to move within the bulk matter, resulting in a relatively large fluctuation in the readout ADC for each channel. Taking electrical tests without bias are necessary due to the need to detect possible defects before continuing past stages in the assembly procedure that remove all further access to certain components.





(a) Amplifier gain for each of the 768 channels

(b) Noise for each of the 768 channels

Figure 11: Readout taken after P-side wire-bonds attached, no bias. In the gain plot a few points can be seen with half the average gain  $\approx 25$ . The group of points are at channel  $\approx 660$ . On the noise plot, these same channels have very high noise compared to the average. This information allows for the classification of defects prior to complete assembly of the detector.

Similarly the peak gain is reduced compared to the calibrated ADC for the injection of 1MIP of charge. This effect arises due to the silicon sensor now being attached to the APV25 channels, resulting in a charge sharing between the APV chips and the silicon sensor. The fraction of charge going to the sensor is related to the effective capacitance of the sensor (sum of capacitance of the load, both sensor and pitch adapter). In order to reduce this effect and provide accurate working conditions to sample from, reflecting those during the Belle II experiment, a reverse bias is applied to the sensor. The application of a bias voltage will drive the capacitance within the p/n junction semiconductor down.

$$C_j = \sqrt{\frac{q\epsilon_s N_B}{2(V_{bi} - V)}} \quad (19)$$

where  $\epsilon_s$  is the permittivity of silicon and  $N_B$  is the impurity concentration of the substrate.

The reverse bias applied to the sensor during the Belle II experiment will be a nominal  $\pm 50V$  and will gradually be increased over the lifetime of the sensor. The increase will reflect the radiation damage sustained by the silicon. The bias required for tracking charged particles is such that the semiconductor is fully depleted. This corresponds to the plateau observed when measuring the variation in leakage current with changing bias voltage.

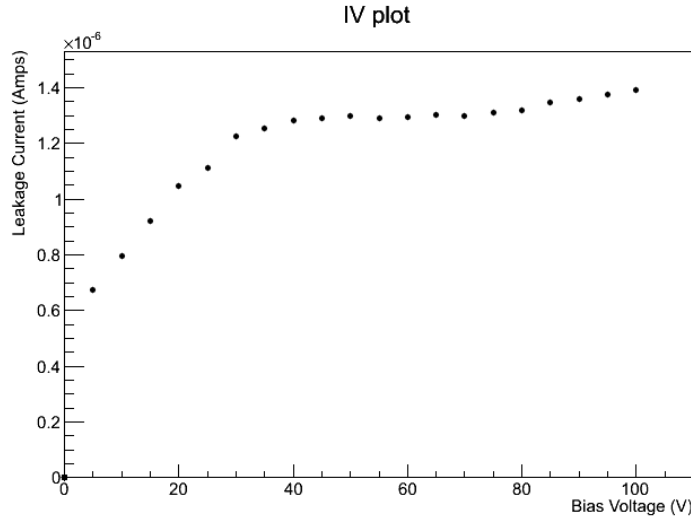
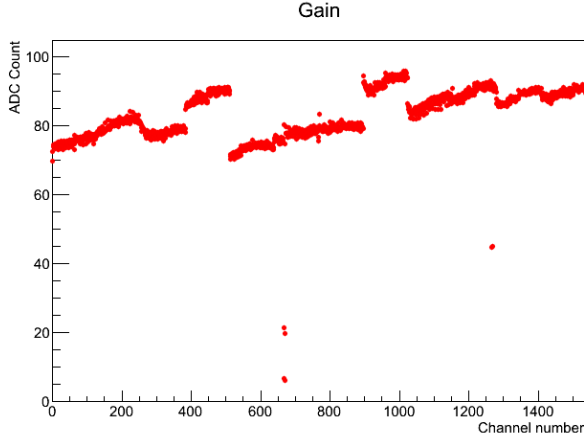


Figure 12: IV plot of L3.001\_fw sensor. Voltage scanned from 0 to  $\pm 100$ V. Plateau clearly visible from 40V onwards with dark current  $\approx 1.3\mu\text{A}$  due to random electron-hole pair creation in the silicon.

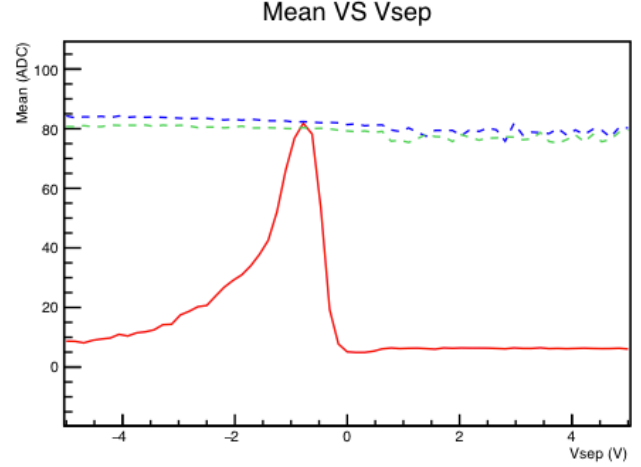
After the final stage of assembly for an SVD ladder an electrical test is performed to evaluate the quality of the ladder under full depletion. The possible defects which are searched for entail:

- Open channel - An open channel corresponds to a channel which is no longer connected to the silicon detector. Usually a result of a bond which has lifted away from the bond pad, was incorrectly bonded in the first place, or a broken wire in the pitch adapter. The characteristics of such a situation include a reduction in capacitance of that channel, due to the removal of the DSSD and the creation of a small capacitor between the floating bond foot and the bond pad connected to the silicon detector (effectively a two plate capacitor). This will result in a large ADC fluctuation on this channel (noise), also the neighbouring channels will have a slight increase in noise due to the electric field generated by the twin plate capacitor. The effect on the internal calibration scan will result with an increased amplitude from the reduced capacitance. For such a defect the ideal solution is to pluck out the bond, if a wirebond is causing the problem. This will remove the electric field driving the large noise in the neighbouring channels. Reducing the negative effect of the damage.
- Shorted channel - A pair of shorted channels are most likely to be incurred during the wirebonding stage of the assembly. A slight misalignment of the wirebonder automated script could result in the bond foot connecting two bond pads. It is also possible for a scratch on the surface of the silicon sensor to scrape aluminium electrode between two channels creating a conductive path. This can also occur if improper care is taken in the cleanroom and metal filings become attached to the surface of the sensor. Such problems are indistinguishable from the electrical testing stand-point and an optical inspection to confirm the position of the short is required. Shorted channels result in an increase in the capacitance for each of the channels involved. This results in the shorted channels having a large noise due to the charge sharing between the channels. The noise of neighbouring channels will remain unchanged as the short is isolated to their respective strips. The gain of each of the channels will halve due to the two fold increase in the capacitance of both channels.
- PIN hole - Channels in which a defect between the  $\text{SiO}_2$  layer situated on top of the  $p^+$  diode are broken. Typically caused during production of the silicon wafers by a piece of dust getting embed-

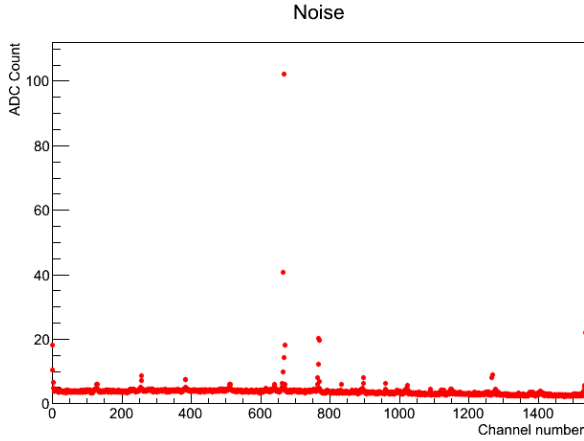
ded between the layers will result in a broken  $\text{SiO}_2$  insulation layer. The effect of the pinholes is that the silicon strips become DC coupled to the APV25. Pinholes can be detected by the increase in noise and gain of the apv25 channel. An additional positive voltage applied to this channel will inhibit the negative current flow into the APV effectively curing this effect.



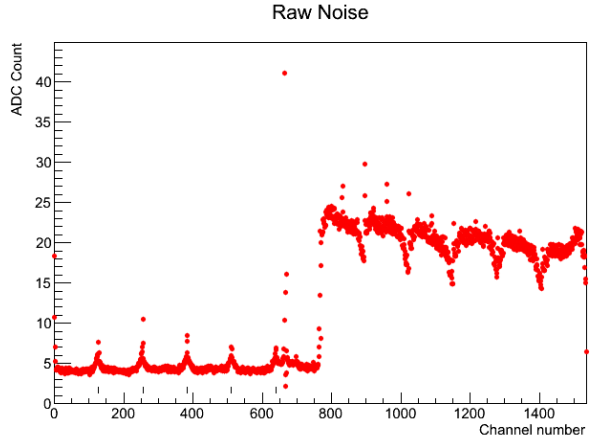
(a) L3.001\_fw gain



(b) A single pinhole detected from the application of additional voltage to the chip



(a) L3.001\_fw noise



(b) L3.001\_fw raw noise

The above results obtained from the L3.001\_fw sub-assemblies contain several electrical defects which may be classified into the aforementioned three classes by observing their physical effects. The gain plot shows that there are several points with a gain much lower than the other surrounding channels. Looking at the corresponding noise plot, we can identify that one of the channels has a very high noise with a couple close channels that are also noisy. This point clearly corresponds to an open channel. Additionally on the gain plot there are a couple of points at channel 1250, both with a gain half of other channels on the chip. From the noise plot there is a slight increase in noise at this point, but isolated to the two channel. This defect is thus classified as a short. Depending on whether the two channels shorted are consecutive, or spaced by one might reveal further information as to the position of the defect on the ladder.

### 6.3 Laser test

Prior to an SVD ladder being classed as suitable for the Belle II experiment the ladder must be verified to be suitable for charged particle detection. This can be performed by injecting a laser pulse into each of the channels of the sensor. If a ladder is to be deemed suitable, 99% of the 3072 channels per ladder must successfully read out the induced signal.

A signal can be induced within silicon by using a 1064nm infra-red pulsed laser. At 1064nm the silicon is almost transparent to the laser, resulting in a uniform creation of electron-hole pairs as the laser pulse traverses the conduction band of the material. By running the laser in a constant motion across the module in the direction perpendicular to the channels, an assessment of quality can be made - paying close attention to total signal distribution, charge cluster size, and uniformity of hits across the sensor.

In order for a photon to be absorbed to create an electron hole pair, the photon energy must be equal to the bandgap energy of the silicon. If the photon energy is greater than the bandgap energy, the additional energy will be dissipated as heat. Light with wavelength of 1064nm will have a penetration depth slightly greater than 320nm making our laser a suitable source for generating photo-current within the channels [7].

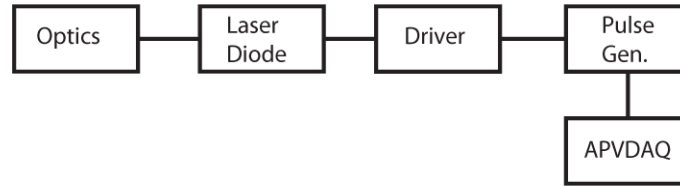


Figure 15: Block diagram of laser setup.

A key component of the research project undertaken was to setup and calibrate a system for assessing the response of the SVD under charge injected by laser.

The laser test system consists of a 1064nm IR diode attached to an elliptical set of lenses with focal spot size of  $< 45\mu\text{m}$ . The optical piece is attached to a DC actuator for precise focusing ( $< 1\mu\text{m}$  step-size) and a DC linear stage for scanning across the finished sensor ( $1\mu\text{m}$  step-size). The laser is pulsed by a pulse generator at 100Hz and a pulse width of 8ns. This corresponds to an instantaneous output energy of  $0.39\text{mW} \times 8\text{ns} = 3.12 \times 10^{-12}$  Joules per pulse. The pulse generator is also used to send an inverted NIM signal to the APVDAQ trigger input.

To assess the response of the silicon detector for both the N and P strips the laser needs to be scanned perpendicularly to both orientations of the rectangular sensor. Due to the carbon fibre ribs attached along the P side of the sensor, a scan across the P strips with this face up would yield a result with two portions of the sensor with no signal generated due to the light being blocked. With this in mind the N side facing up is used when scanning across both N and P strips. The drawback to this is the polyimide (Kapton) pitch adapter covering  $\approx 60\%$  of the sensor surface. The polyimide reduced the transmission of the IR laser through the sensor, result in a reduced signal readout B.

In order to read out the signal being induced by the laser, a carefully timed trigger must be sent to the APV25 chip that coincides with the memory cell storing the signal generation in the detector. The difference in timing between the trigger request and signal generation will be due to the delay caused by travel time in the electronics and cabling.

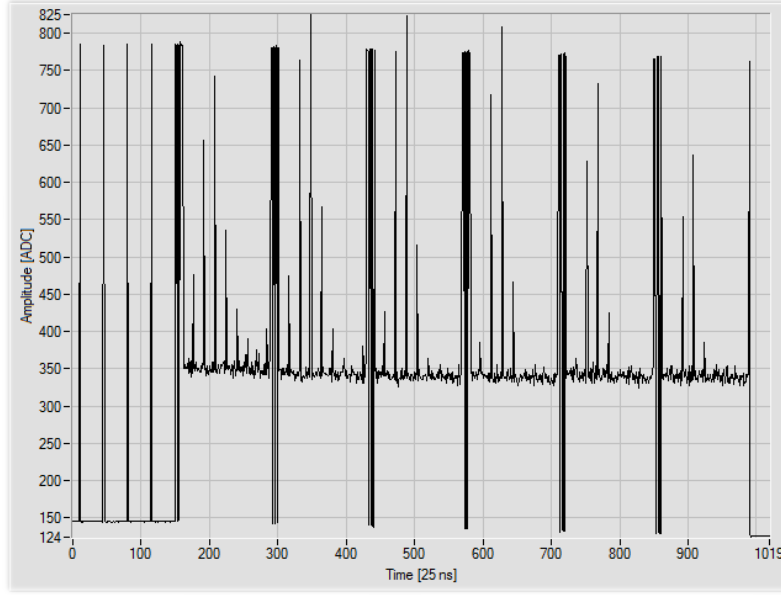


Figure 16: Realtime ADC output from APVDAQ software. Each of the thick black lines denotes a clock cycle. Occuring every 25ns. The spacing between the clock cycles displays the ADC of each 128 readout channels for the displayed chip.

Trigger timing can be established by systematically varying the delay between the pulse sent to the laser driver and the pulse sent to the external trigger input of the APVDAQ. As the delay is increased the trigger request sent to the ring-buffer on the APV25 will coincide with a sample at a point  $N \times 25\text{ns}$  ahead. Operating in multi-peak sampling mode, the trigger is delayed such that the output coincides with six samples along the peak of the output signal pulse. When the trigger coincides with the memory buffer cells containing the signal the expected landau charge collection distribution will be seen in the ADC across the six clocks.

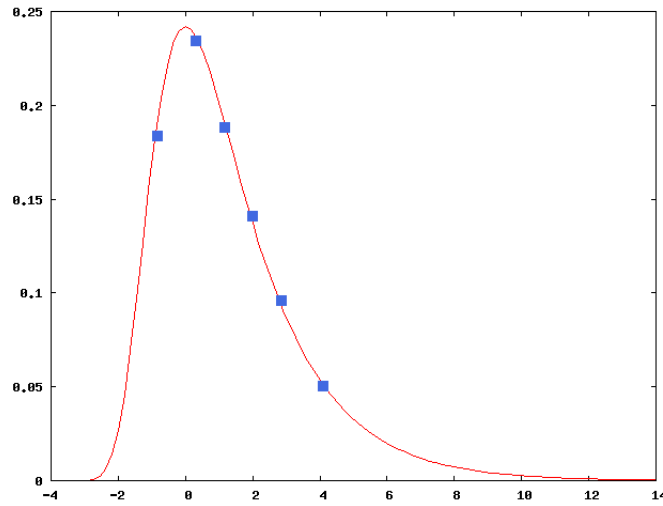


Figure 17: Trigger is timed such that the output is focused around the peak of the collected charge distribution

Of the six sub-events recorded per trigger only the three maximum signal points are used in the cluster analysis. These maximal points correspond to primary charge collection created when an ionising particle passing through the material.

## 6.4 Laser Results

Following the design, set-up and calibration of the laser scanning system and creation of the analysis software. The following results were taken from the L3.001 SVD ladder as part of the quality assessment procedure. For the P scan the laser is scanned across the sensor at a rate of  $50\mu\text{m/s}$  and the N side at a rate of  $160\mu\text{m/s}$  with the laser pulsing at 100Hz in both cases. Resulting in 100 injected pulses per channel.

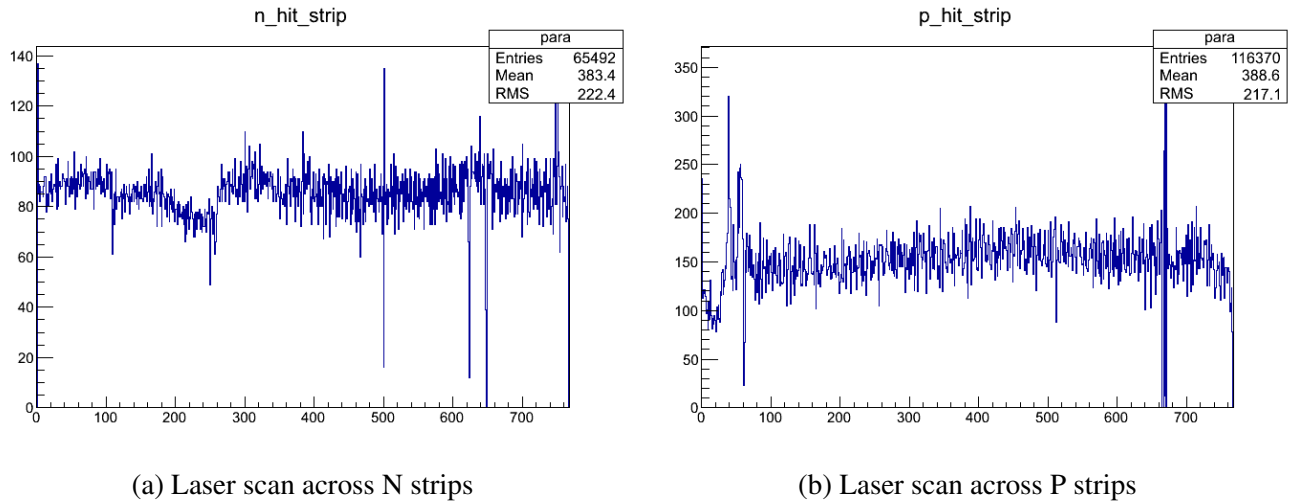


Figure 18: Laser scan results for L3.001\_fw ladder, the number of hits recorded for each channel passing a SNR cut of 3.

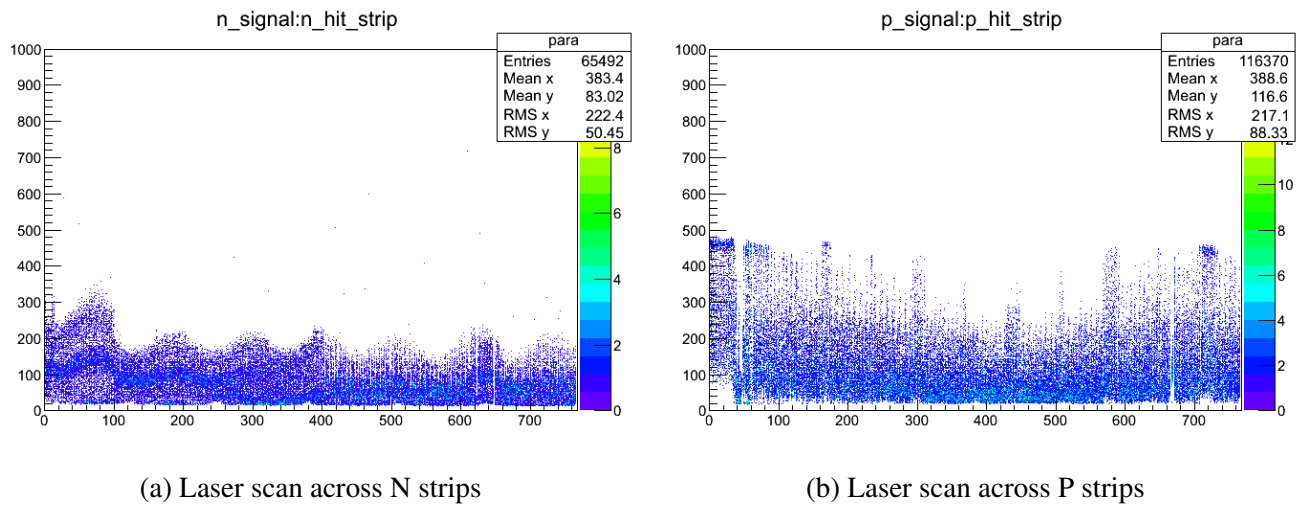


Figure 19: Laser scan results for L3.001\_fw ladder, the signal distribution measured within each channel is shown

The N side hit scan reveals a drop-off in signal generated from hits in channel  $\approx 250$  onwards. This coincides with the position of the polyimide pitch adapter on the surface of the sensor. The periodicity of the signal distribution is a result of a small angle in the path of the laser's motion. The small angle causes the centre of the intensity profile of the laser to occasionally be blocked, completely, or partially by the Aluminium electrodes parallel to the laser's path. As such, the intensity of the laser passing through the sensor is reduced. The effect is more evident for the scan across N strips due to the smaller pitch of the P strip electrodes [26].

Additionally defective channels can be identified from the signal distribution of the sensors. On the p-side scan channel  $\approx 680$  has zero recorded hits and no signal. This matches up with the electrical result shown in 13a, where an open channel was detected. The open channel does not collect any charge from the sensor and as such will not respond to the injected laser pulse. Similarly channel 650 on the n-side has zero recorded hits and an absence of signal. This is a result of the short between the two channels, see 13a. The shorted channels do not read out the induced signal as a result of the large capacitance inhibiting the amplification of the signal.

## 7 Silicon Clustering

The laser scan outlined in 6.3 is a key component of the electrical assessment of the silicon modules. The readout of a measured signal provides the information necessary to determine if each of the silicon strips are functioning properly. Compared to the electrical test which purely provides a means of investigating the electronics and the capacitance of the sensor to some extent. The laser test directly creates electron-hole charged carriers within the depletion band of the silicon. Creating a situation similar to that in which the ladder will be used during the Belle II experiment, measuring ionisation due to interaction with charged particles.

In order to measure a signal response in each of the 768 channels per side per detector an automated system must be used to systematically produce a signal within each strip. Uniform generation of signal within each of the channels allows for assessment of detector response by comparison of relative signal within each of the channels.

An understanding of the possible variability of the laser signal setup and the resultant affect on the created clusters within the silicon is vital in understanding the signal readout.

### 7.1 Internal reflections from laser signal

When performing a study on the uniformity of signal response using a scanning laser system, a problem that is likely to arise is one of internal reflections. The internally reflected light will create additional electron-hole pairs as the light continues to travel through the silicon. The resulting cluster will appear much larger in size (number of strips charge collected on) and shape (2D hit map on N and P strips) compared to the single illuminated strip of depth  $320\mu\text{m}$ . This need not necessarily be a problem if the internal reflection remains constant across the entire sensor, maintaining uniformity of the signal creation. However this is something that is difficult to ensure, due to the internal structure of the sensor. A small variation in electrode implant depth, or a warping of the sensor would locally change the angle of internal reflection. The best way to deal with this problem is to eliminate the reflections entirely.



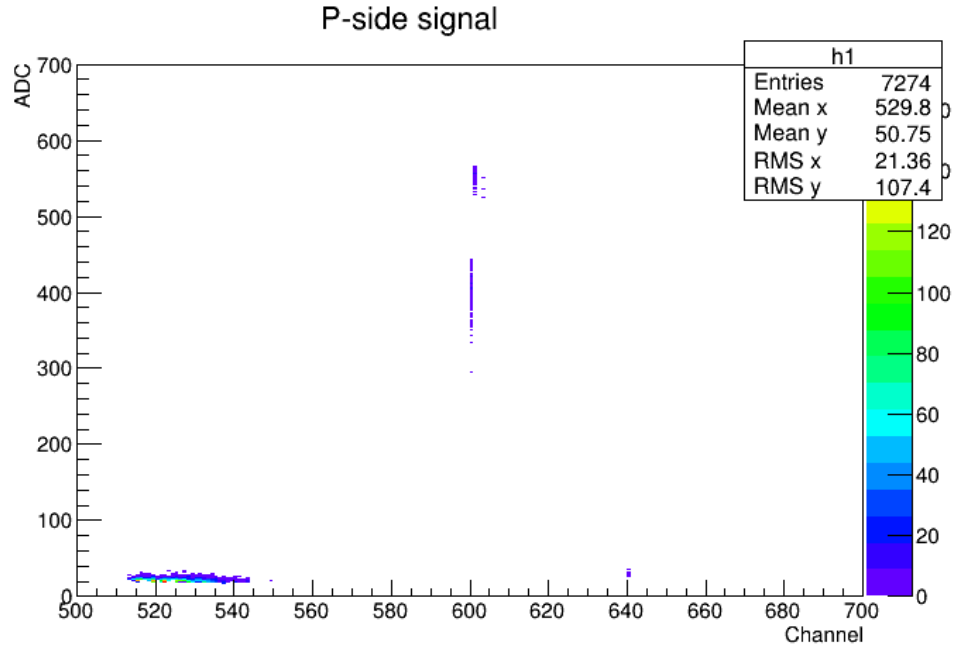


Figure 20: Internet reflections inside the silicon sensor. The large cluster around channel 520-540 is the reflected laser pulse

The following sample was taken from the L3.001\_fw module. The energy of the laser output was varied over an energy range corresponding to pulse widths of 8 to 20 ns. For each sample the charge contained within the reflected cluster was calculated.

The conditions for reconstructing a cluster are as follows: The strip with the highest local SNR is found, the SNR of the neighbouring channels are checked to see if  $\text{SNR} > 3$ , each additional channel neighbouring channel with  $\text{SNR} > 3$  is added to the cluster, neighbours are added until there is no neighbour within 3 strips from the last with a  $\text{SNR} > 3$ , the cluster charge is then calculated as the sum of the signal of each of the channels in the cluster. An additional check is made to ensure that each channel with  $\text{SNR} > 3$  has a corresponding strip on the opposite side with  $\text{SNR} > 3$ .

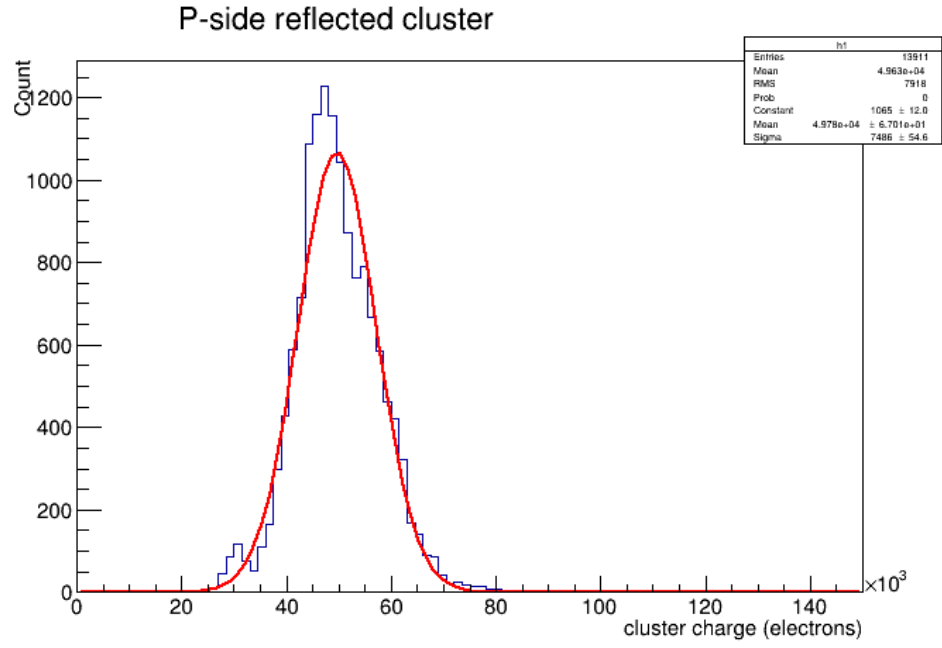


Figure 21: Reconstructed cluster charge collected on the p-side

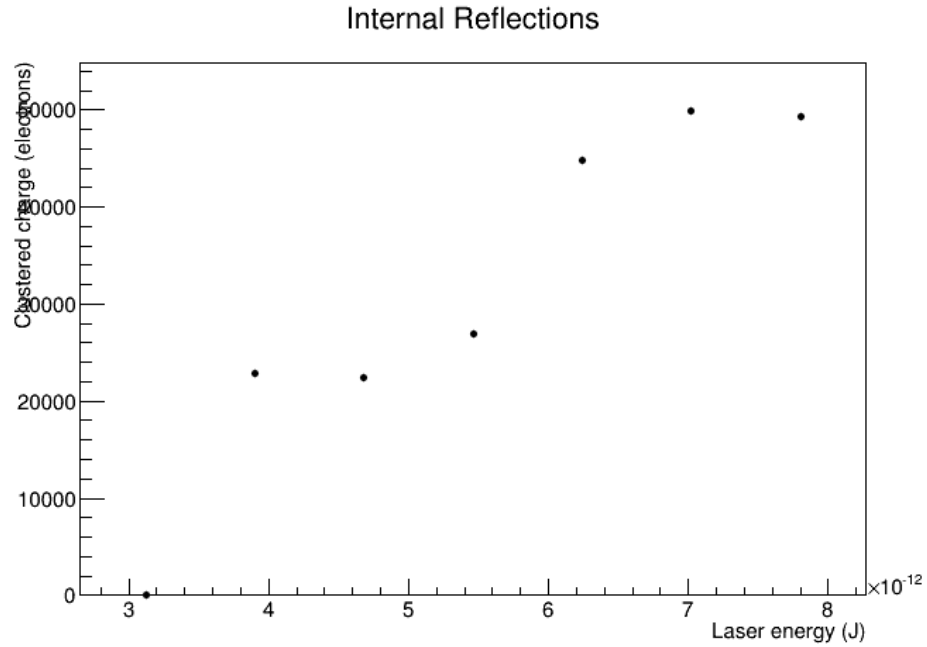


Figure 22: Charge contained in reflected clusters vs energy of laser pulse

As shown in [7] the transmission of 1064nm light through Si is  $\approx > 320\mu\text{m}$ . By decreasing the energy of the laser output, a reduction in the charge of the reflected cluster until a threshold is reached at  $3 \times 10^{-12}$  J

## 7.2 Angular laser injection

The Belle II SVD is designed to measure the trajectories of charge particles passing through the active volume. As the particles cross the volume, they lose energy by creating electron hole pairs, these pairs then drift under the effect of the bias voltage. When a magnetic field is applied, the charge carriers now experience a Lorentz force. This results in an angle between the motion of charge carriers and the electric field.

Correct calibration of the Lorentz angle is necessary in order to reduce the size of the measured clusters resultant from charged particle tracks, and improve the spatial resolution of the cluster position. While negligible for tracks passing through the detectors parallel to the Lorentz angle. With proper consideration of the Lorentz angle, track reconstruction performance may be improved, ??.

An approach to making this measurement would be to inject charges at the surface of the silicon detector and observing the drift of the charges by measuring the position of the charge on the other side [8]. Alternatively by measuring the size of the cluster created when a laser pulse is injected with various angles of incidence. A minimisation in the cluster size will be correlated with an angle of incidence equal to that of the Lorentz angle.

Although the calibration of Lorentz angle goes beyond the scope of this paper. A survey of the viability of an angular laser injection calibration procedure has been included due to the overlap with small angle clustering.

The following sample was taken from the L3.001\_fw module. For each measurement the laser (beam width  $45\mu\text{m}$ ) was refocused to account for the increased pathlength due to the angle of inclination.

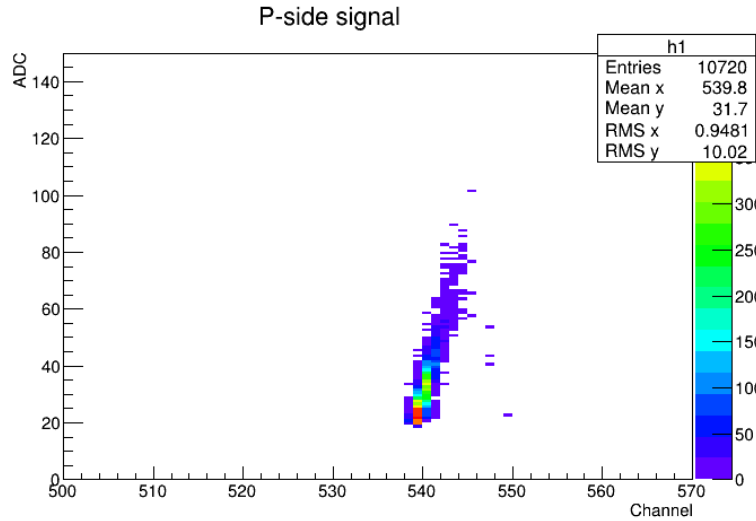


Figure 23: Signal distribution of cluster. Angle of 30 w.r.t normal at the surface

The laser was position at various angle with respect to the P-side strips (pitch  $50\mu\text{m}$ ) with the sensor at full depletion and 6000 events were recorded. The spatial size and collected charge of the resulting clusters were then reconstructed.

The resultant charge collected in the induced cluster is determined as outlined in section 7.1.

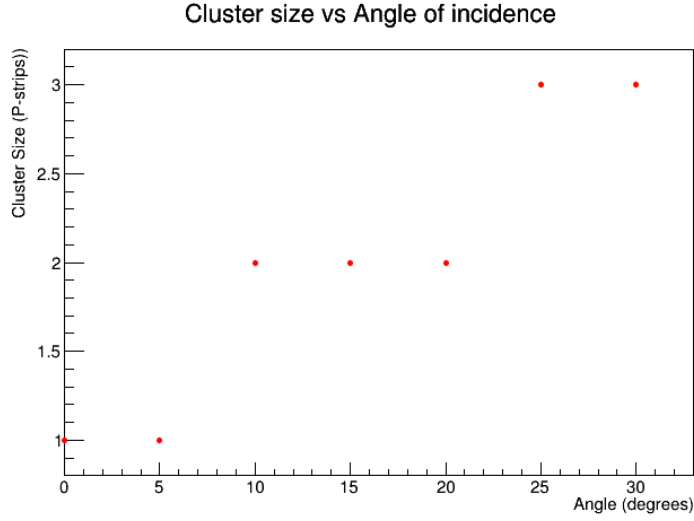


Figure 24: Cluster size found for varying angles of incidence

The cluster size was calculated by removing the channels with number of hits less than 5% of the number of events. This gave the most probable cluster size. The resulting cluster size as shown in the above figure matches the expected relationship between angle and cluster size.  $x = y \sin(\theta)$  where  $x$  is the length in the direction across the pitch of the strips and  $y$  is the thickness of the silicon ( $320\mu\text{m}$ ).

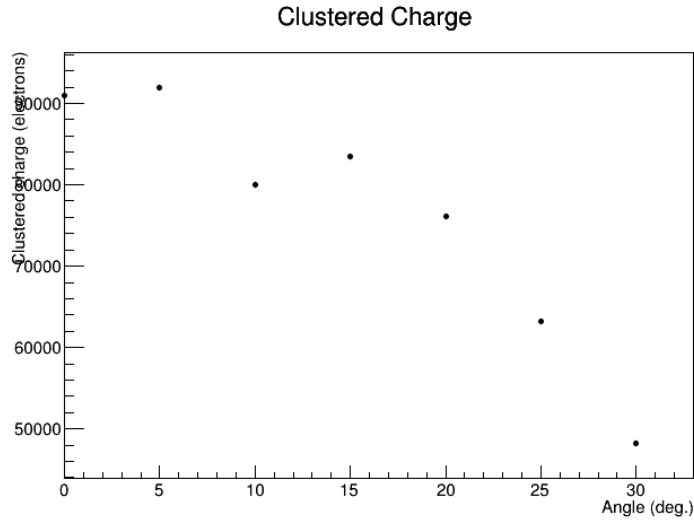


Figure 25: Charge contained within created cluster for varying angles of incidence

The charge associated with clusters created with injected laser at various angles is expected to increase with increasing angle of incidence. This is due to the signal created within the silicon being proportional to the distance the ionising laser pulse travels, so long as the distance is less than the absorption length. A possible explanation of this effect may be related to the ratio of beam-spot size and the pitch of the P-strips. The distance between the centre of two parallel aluminium implants on the P-side is a nominal  $50\mu\text{m}$ , with the width of the aluminium implant  $\approx 16\mu\text{m}$  and silicon  $\approx 34\mu\text{m}$ . When the laser spot is

of a comparable size  $45\mu\text{m}$  FWHM, there is going to be a narrow region where the intensity of the laser penetrating the silicon is maximised.

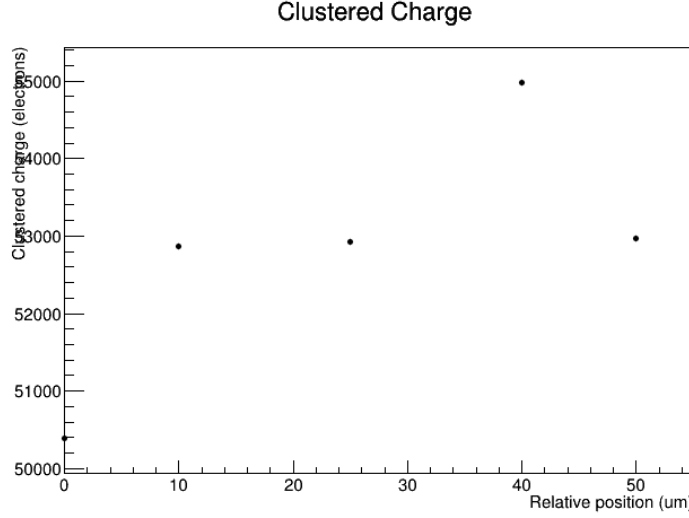


Figure 26: Amount of charge created at different points across the pitch of a strip

Taking cluster measurements in small discrete steps across a single p-strip a variation in clustered charge was detected. A variation of up to 10% was seen to occur depending upon the position of the laser with respect to the strip. When an angle is introduced the laser spot on the surface of the silicon will appear elliptical, smearing the intensity profile of the beam over a larger surface.

However the dominant process causing the reduction in charge, hence reduction in intensity passing through the silicon will be reflection. The refracted component of the beam  $n_1 \sin(\theta_1) = n_2 \sin(\theta_2)$  where  $\theta_1$  is the angle with respect to the normal at the surface and  $\theta_2$  the refracted angle. The intensity decreases due to Fresnel loss with a reflection coefficient  $R = \left(\frac{n_1 - n_2}{n_1 + n_2}\right)^2$  [7]. For  $\text{SiO}_2$  with refractive index of  $\approx 1.9$  the transmission coefficient at an angle of 30 from air with  $n=1$  corresponds to 0.45.

### 7.3 Cosmic muon calibration sample

In order to assess the quality of the silicon detector for weakly ionising particle detection a cosmic muon sample was measured. The mean energy of cosmic muons measured at the earth's surface  $\approx 4\text{GeV}$  [10], this corresponds to a  $\beta\gamma$  of 38.07 from these muons approximately correspond to a minimally ionising particle, to the order of a few percent. These events correspond to the lowest ionising events that the SVD will be measuring when the Belle II experiment begins.

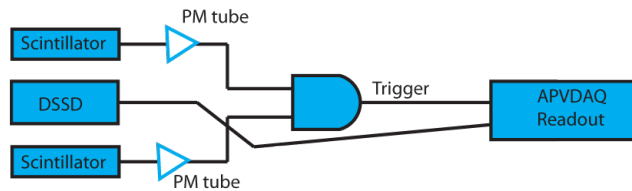


Figure 27: Block diagram of setup used to measure cosmic muons

The pair of scintillator pads with an area of 100mm by 160mm, enclosing the silicon detector were used as a trigger for timing of the muon passing through the sensor. Muons with a large angle of incidence to the detector were rejected due to the limited size of the pads. The detector itself only occupying  $\approx \frac{1}{4}$  of the scintillator collection appature, with a portion extending beyond the scintillator pads. This resulted in a collection rate of  $\approx \frac{1.4}{4}$  events per second.

Following a sampling time of five hours 5466 muons were detected by the L3.001\_fw sensor.

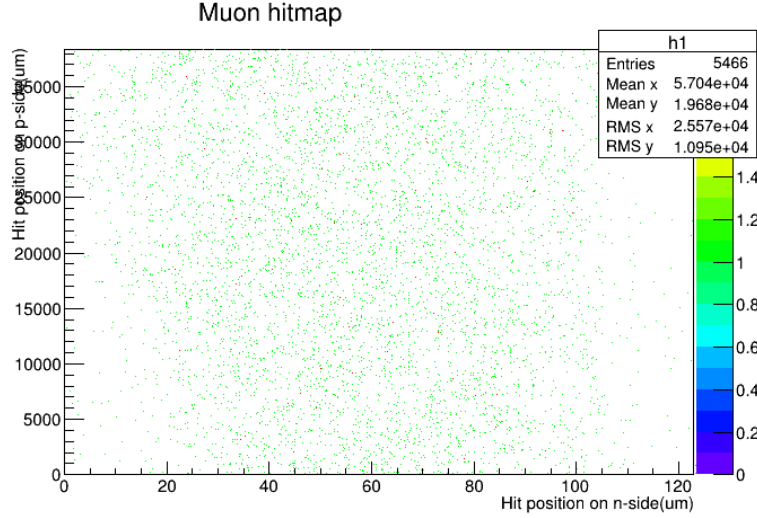


Figure 28: Two dimensional hit map of cosmic muons passing through the L3.001\_fw sensor

The map of detected hits lacks any spatial correlation, consistent with the cosmic data sample. It can also be seen that very few muons are detected at the very end of the detector (N side hit position  $> 120 \times 10^{-3} \mu\text{m}$ ), this is due to the sensor extending beyond the range of the scintillator pads. Any muons passing through this region will not induce a signal within the scintillator and thus no trigger will be sent to the readout chip.

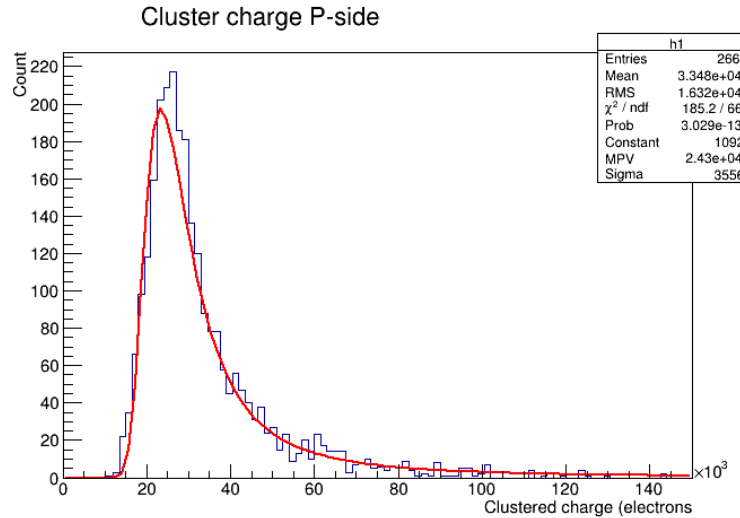


Figure 29: Charge collected from a cosmic muon passing through the P side of the L3.001\_fw sensor

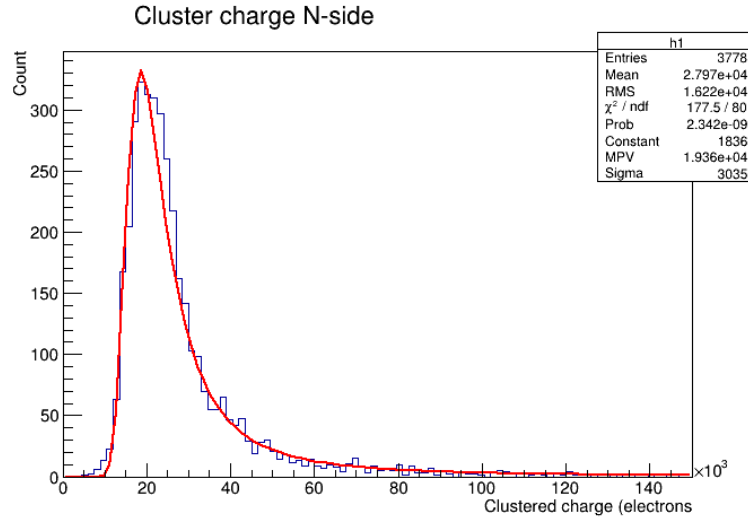


Figure 30: Charge collected from a cosmic muon passing through the N side of the L3.001\_fw sensor

The reconstructed cluster charge created by the ionising muon is consistent with the charge distribution expected with a MIP like signal. The charge clearly takes the form of a landau distribution with a most probable value of 24300 electrons measured on the P side and 19360 electrons measured on the N side. These values are quite close to the nominal value for a MIP  $\approx 24000$  electrons. The discrepancy between the values may be due to poor calibration of ADC to collected charge. The calibration settings used for the sample are based on the internal calibration circuit which are based on capacitances. The capacitive based calibration is not a very reliable calibration source. With a correct calibration for ADC to collected charge the measurement should better reflect the nominal value.

## 8 Low momentum tracking improvements using dE/dx

Ionisation energy loss in material detectors (dE/dx) provides a means for identifying particles by exploiting the difference in energy deposition of different particles for a given reconstructed momentum.

When calculating the mean dEdx a common method for truncating the mean of the Landau distribution for a given track is to remove the highest and possibly the lowest valued hits for that track. This can have significant distortion of the mean for low momentum tracks in the SVD(VXD) that only contains typically 4(6) clusters, where dEdx increases as  $\frac{1}{\beta^2}$  with decreasing momentum.

Particle tracks in this low momentum region will have a small radius of curvature within the magnetic field. Some of which accumulate additional hits in the SVD if the radius of curvature is smaller than the radius of the outer svd layer. Additionally some tracks passing into the CDC may return depending upon the significants of multiple scattering. These additional clusters provide a means of gaining additional data for calculation of the dEdx truncated mean. Greater statistics in the calculation of truncated mean will improve the value and the efficiency for which particle identification can take place.

While such a study is impracticable to undertake using real reconstructed data. The significance of the additional information result from this survey may provide motivation for extending the ideas presented in improving the tracking efficiency of low momentum tracks.

### 8.1 $D^*$ data sample

A process of key interest in B physics is the decay of the B meson into a  $D^*$ , an orbitally excited D meson with a branching ratio  $B \rightarrow D^*(2010)^\pm X = 22.5\%$  [10]. Where X refers to any possible particle for this decay.  $B \rightarrow D^*\tau\nu$  and  $B \rightarrow D^*K$  are both a set of important decay modes in which expected new physics is to take place[4]. A precise reconstruction of the  $D^*$  is fundamental to measuring the branching fraction. The key to measuring these decays is the reconstruction of the  $D^*$  which decays into  $D^0\pi$  with a branching ratio of 67.7%. As a result of the small mass difference between the  $D^*$  and the  $D^0$  (146MeV) the pion of mass 140MeV will have very little momentum phase space available and as a result the  $D^*$  decay. If the slow pion is not found at all by the track reconstruction a large portion of the  $D^*$  decays may be incorrectly reconstructed. If the charge pion is not found its charge information is also lost which might result in the incorrect charge reconstruction of the grandparent B meson.

Additionally many difference analyses it can be useful to fully reconstruct one of the B mesons (tag) to constrain the four-momenta of the second B meson (signal). This can be used to simplify the reconstruction of the signal B, especially where a neutrino exists in the final state. Because of the high branching fraction of the  $D^*$  production it is important that the  $D^*$  is correctly reconstructed. This involves correctly finding and identifying the  $D^0$  decay products, aswell as the second particle produced in the  $D^*$  decay.



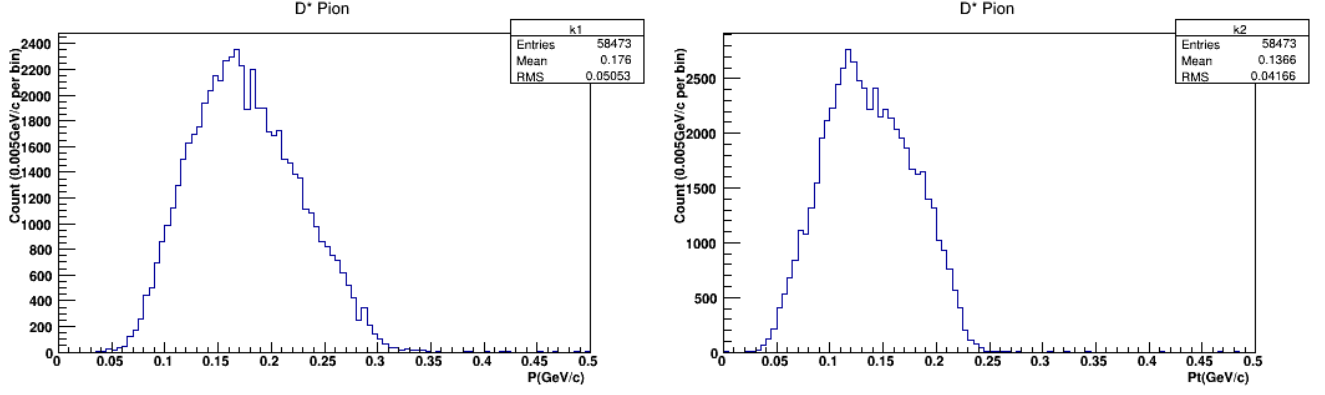


Figure 31: Reconstructed momentum and transverse momentum for slow pion

## 8.2 Belle II simulation

The Belle II analysis software framework (BASF2), provides two regimes for generating the production of particles. The first is the aptly named ParticleGun module. This module allows the user to shoot various particles into the detectors with controllable kinematic and spatial parameters. The benefit offered by this module is being able to directly control the particle being simulated. Allowing for study of detector response, or reconstruction efficiency for different particle configurations. The second method is the more realistic approach, simulating the decay of a pair of  $B^0\bar{B}^0$  or  $B^+B^-$  from the  $\Upsilon(4S)$  resonance. This is performed by the EvtGen module[16], designed for the simulation of B meson decays. The follow on decays from the B pair can be selectively generated using decay files, a system for creating decay chains to stable final states from allowed decays. Following the generation of the particle and its subsequent decay each of the subdetector hits are assigned to the monte carlo particle they were generated from and are held as hit candidates. The tracking is performed independently for each of the subdetectors. For hits in the VXD, tracking is performed by the VXDTF which undergoes pattern recognition to create a list of track candidates. The tracks in each of the subdetectors are then merged and processed by GENFIT, resulting in track objects that contain reconstructed track information, vertex position, momentum and charge.

## 8.3 dE/dx from trackfit parameters

The dEdx of a specific track can be calculated from the energy deposited within a subdetector hit and the reconstructed pathlength of the particle passing the medium. The energy deposited information is stored in both the reconstructed cluster class SVDClusters and the truth class SVDTrueHits. SVDClusters are produced from the SVDDigits (converted simulated energy deposited into detector response of single strips) by performing 2D clustering in strip coordinate and time. SVDTrueHits are particle hit data from the geant4 simulation. The reconstructed path length through the silicon can be determined by assuming an ideal helix from the reconstructed position and momentum at the point of closest approach. The helix allows for the momentum at the surface of the svd hit to be used to calculate the angle of incidence into the silicon. An approximation of path length as a straight line inside the silicon is given by  $x = \frac{d}{\cos(\theta)}$ , where d is the thickness of the silicon [17]. This method provides a close approximation for negligible energy loss and multiple scattering.

A simulation consisting of 10000  $D^* \rightarrow D^0\pi$  decays generated and the truncated mean dEdx of the slow pions calculated. In the truncation calculation the top 25% dEdx values were track were removed

prior to averaging.

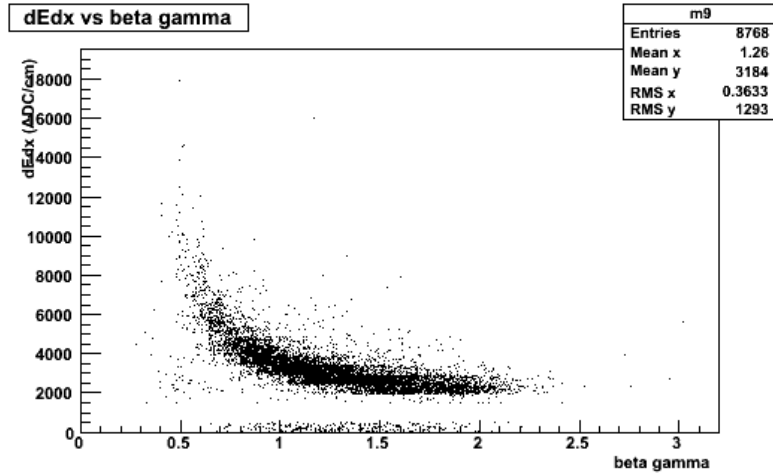


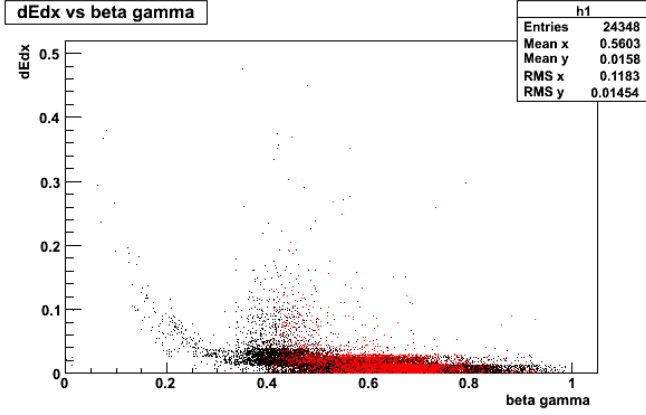
Figure 32: Truncated mean dEdx vs beta gamma for slow pions from  $D^*$  decay

## 8.4 Curling tracks in the SVD

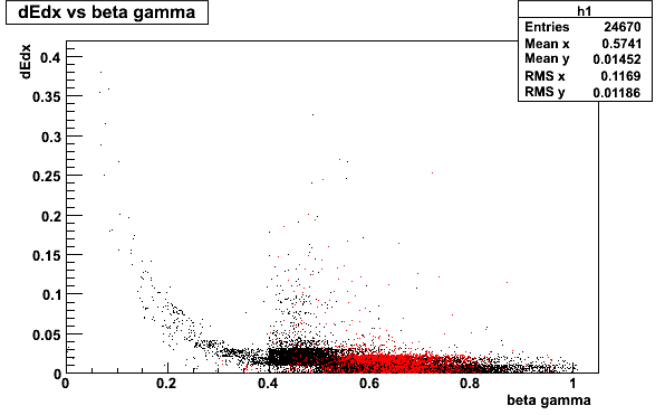
Particles with a transverse momentum below 70MeV have a radius of curvature of 14cm in the absence of energy loss and negligible multiple scattering. Such tracks are confined to within the SVD, all hit information is contained within the VXD (Pixel detector + SVD). As shown in fig. the mean transverse momentum of the slow pion is 136MeV. A significant portion of these will be contained to within the SVD. Although the tracks may be contained within the SVD, curlers will only result if the track has a low momentum in the direction of the beam. Additionally, tracks which extend beyond the SVD and into the CDC, may curl back into the SVD as a result of scattering in the CDC. As the *VXDTF* module only searches for track candidates propagating outwards from the beam, hits from curling tracks, track which curl back into the SVD subdetector are rejected as hit candidates for the track. Additionally in the low momentum region the efficiency of track fitting is reduced due to large energy loss taking place within each of the SVD layers. The large momentum loss results in the momentum loss stepsize in the Kalman Filter contained within GENFIT. Leading to a rejection of the hit in the track fit.

As a result of the trackfinding not searching for curling hits, the trackfit parameters used in sec. are no longer available to reconstruct the dEdx of the hits, nor find the hits. As this study is not extendible to real data reconstruction, it is simply to see if possibility for improvement to PID exists from collection additional hits from curlers. With this in mind *SVDTrueHit* information is used to the position of hits from a curling track and its dEdx. Notable the *SVDTrueHit* class stores information on the entry and exit position of the particle passing through the volume, the 3-momentum at the entry and exit, and the energy deposited within the medium. The dEdx can be calculated by dividing the deposited energy by the length of the path from entry to exit position. The detection of additional hits as a result of curling tracks is undertaken as follows: for a reconstructed track to final hit, at this point the exit momentum of the hit is used to create an ideal helix path see C, search through all hits stored in the *SVDTrueHits*, calculate the difference between the fitted helix path and the hit, take the closest point to the track with a difference in position less than a threshold set (calibrated by measuring the difference between fitted track points and helix fits from true exit momentum), continue to pick up points until no close points are found.

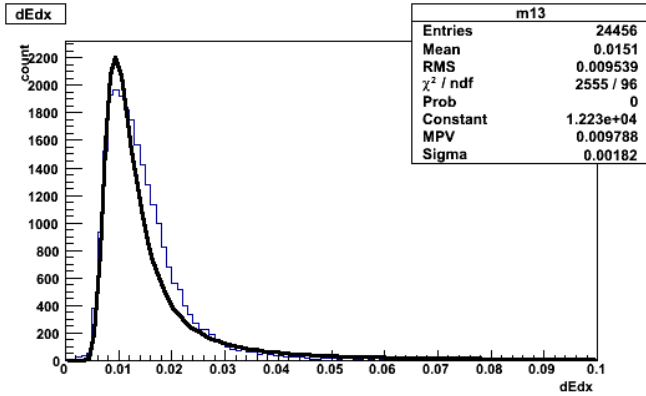
ParticleGun was used to create pions with a normal momentum distribution with mean and sigma  $70 \pm 20$  MeV. The pions were fired in a uniform theta direction from 85 to 95 degrees. This configuration is chosen to increase the number of tracks that curl back into the SVD layers. The simulation was performed with both VXD and SVD hits used as hit candidates for the VXDTF and SVD hits only for the VXDTF. VXDTF requires atleast either 2 PXD and 1 SVD hit or 3 SVD hits to form a track candidate.



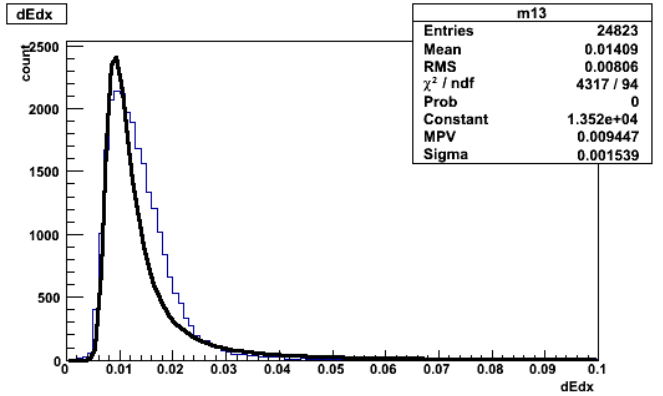
(a) With pixels



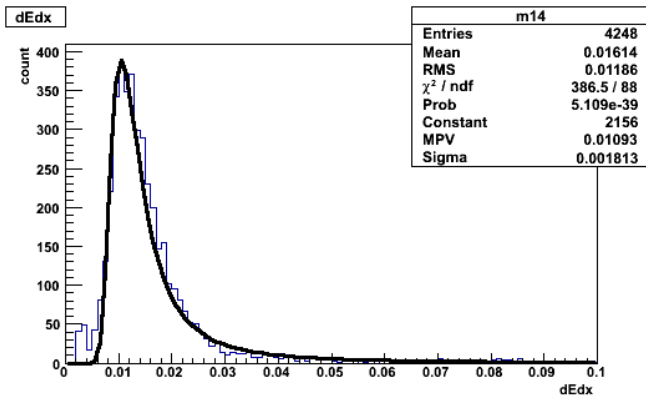
(b) SVD only



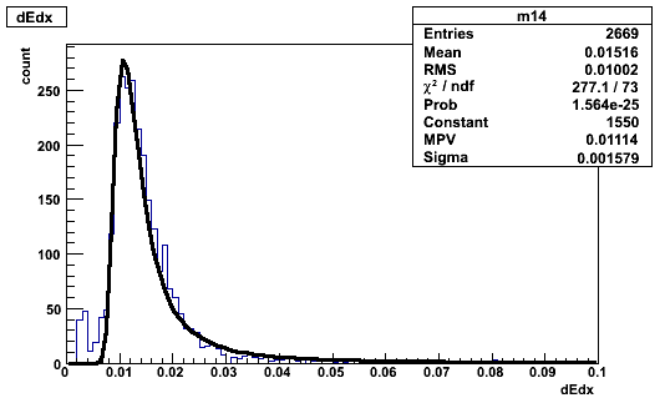
(a) With pixel



(b) SVD only



(a) With pixel



(b) SVD only

The first set of plots show the on reconstructed track dEdx using truth energy deposit information in black and the additional hits captured along the helix in red. The first pair of dEdx distributions are for

the on track hits, the second pair the hits found along the curling track. Comparing the curling hits dEdx distribution to the track fit hits, a slight increase  $\approx 10\%$  in dEdx is seen. This, however the result is less significant than one would expect when looking at low momentum track with energy loss  $\propto \frac{1}{\beta^2}$ . This may be a result of the low number of curling tracks compared to the number of events generated. With six times as many hits belonging to the hits of the tracks exiting the SVD volume. There is no observable benefit between using SVD only hits, or SVD+PXD in the track finding. The pair of dEdx vs  $\beta\gamma$  plots reveal a deceptive double band structure, similar to the dEdx distribution of a mixed particle sample. This however is not the case, rather the very low momentum track hits that don't reach the external layers of the SVD and are absorbed within the layers exhibit the  $\frac{1}{\beta^2}$  structure at  $\beta\gamma < 0.2$ . The  $\beta\gamma$  for these plots are based on the reconstructed track momentum at the reconstructed vertex point. If instead we plot the dE/dx against the  $\beta\gamma$  of the particle just before interacting with the matter.

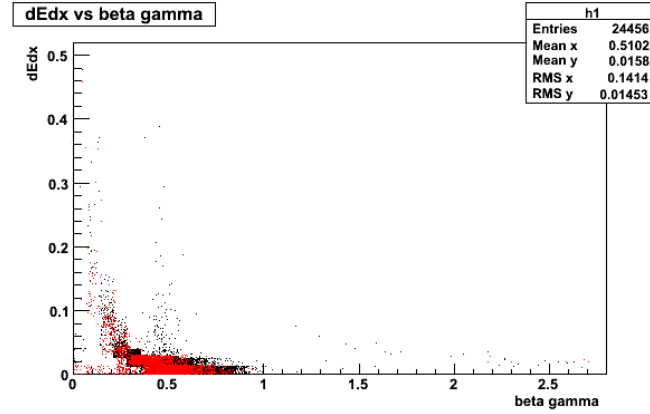


Figure 36: dEdx with updated beta-gamma

The updated  $\beta\gamma$  reveals that the curling tracks do follow the same energy loss distribution as the very low momentum tracks that do not reach the outer layers of the SVD and are absorbed in the medium. From this information we can see that the curling tracks provide similar energy loss information as very low momentum hits. Increasing the number of points available in the low  $\beta\gamma$  region. Therefore by collecting the points corresponding to hits from curling tracks we can get a better resolution for dE/dx. The problem remains that the number of curling tracks found in simulation, even when using truth to reconstruct each helix effectively, is rather low.

## 9 Conclusion

It has been thoroughly shown that the electrical quality assessment procedure detailed through this thesis is an efficient and successful means of identifying defects during SVD production. At different stages in the assembly defects such as shorted channels incurred during the wire-bonding stages can be identified without difficulty. After the module is completed and bias voltage is supplied to fully deplete the sensor, a full assessment can be performed upon the ladder to evaluate if the component is suitable to partake in the Belle II experiment.

The laser system was designed, calibrated and analysis software created for verifying the electronic response in the silicon. A complete survey of the laser signal generation within the silicon detector was conducted paying attention to the variables related to the laser scan as part of the procedure. To confirm if a layer is fully suitable for experiment it must be out to successfully read out a signal generated within the silicon strips.

The laser system was further analysed to determine if angular variations could be detected within the p-strips of the silicon detector. The reconstructed cluster size for various angle of inclination was studied and suitable performance was found for using the laser system in a Lorentz angle type measurement.

Analysis of low momentum particle tracks resulting from slow pions was studied as a sample for improvement of  $dE/dx$  resolution improvement. It was found that the additional hits from curling tracks had  $dE/dx$  values similar to those of the lowest momentum pions, allowing for improvements to be made.

## A Laser optics

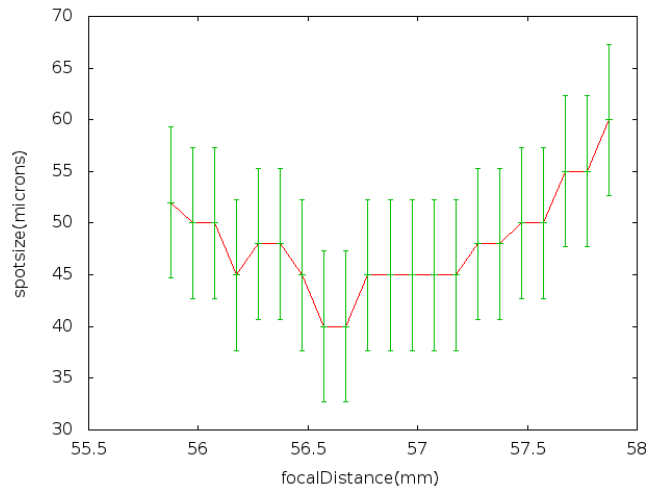
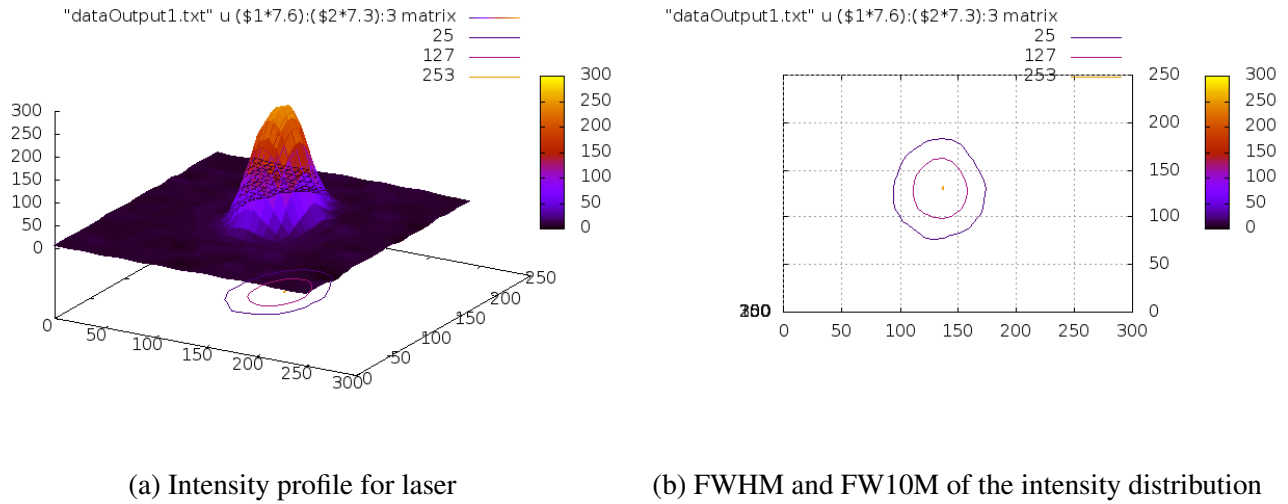


Figure 38: Focal width of the laser

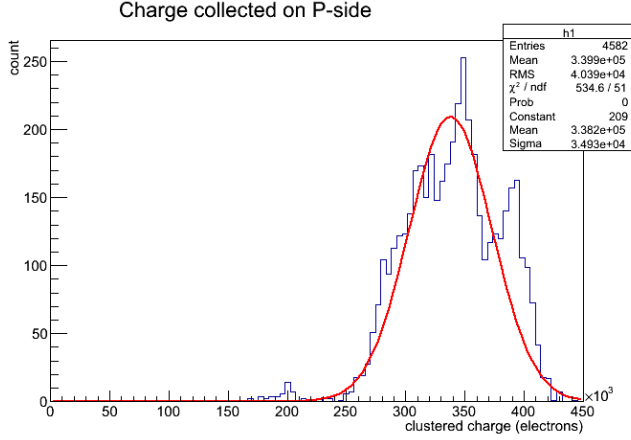
To be able to perform any of the laser tests described in the preceeding sections a detailed understanding of the laser beam profile is necessary. A well focused laser with spotsize below that of the pitch of the silicon sensors allows for single strip illumination and thus knowing the position where the charge originates.

The laser was injected into a CCD with the output digitised with a resolution of 720x576 pixels. To map the beam profile software based on openCV was used to fit contours using a caneyfilter to the beam size and map the intensity.

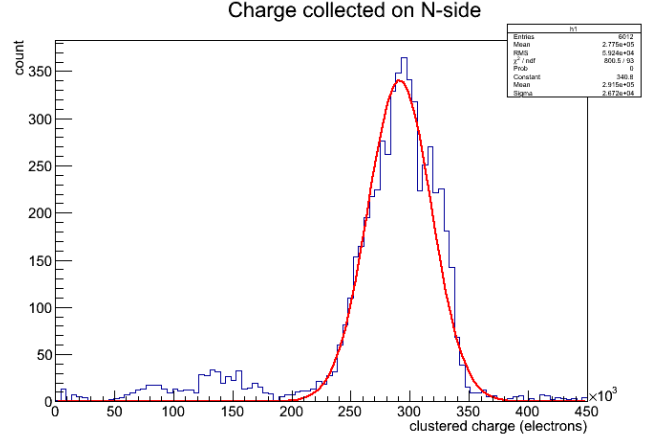
The intensity profile of the output data correctly matches the gaussian profile. Varying the distance between the CCD and the laser the focal position was found and beam profile mapped, taking measure of the Full Width Half Maximum and the Full width 10% Maximum to see the degree of the tail of the profile.

The focal depth of the intensity was measured to ensure that the beam may pass through the silicon without broadening too much, making single strip analysis difficult.

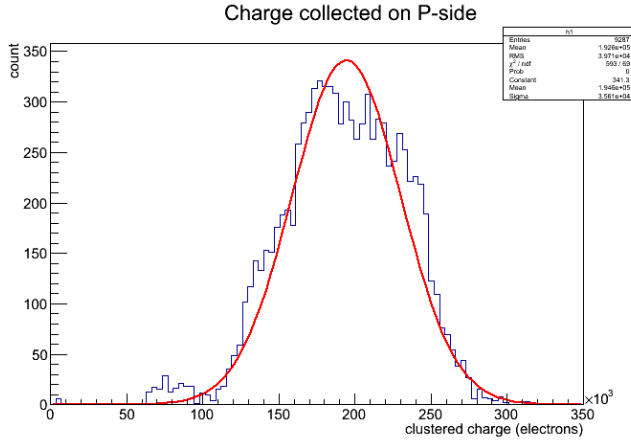
## B Polyimide IR absorption



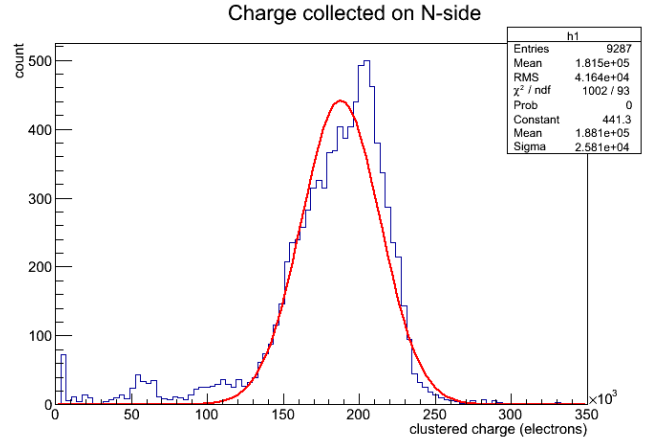
(a) P side cluster no PA



(b) N side cluster no PA



(a) P side cluster PA



(b) N side cluster PA

Approximately a 30% reduction in clustered charge when the PA is between the laser source and sensor.

## C Helical coordinate system

Charged particles moving within a magnetic field trace out helical paths as a result of the Lorentz force acting upon the particle. Assuming a uniform, homogeneous magnetic field and negligible multiple Coloumb scattering, the tracks will be near perfect helices. The track at any point in time can be described by a set of 6 space and momentum parameters  $(x, y, z, p_x, p_y, p_z)$ . However this be reduced to a set of 5 parameters using the perigee helix representation [18]. The perigee representation consists of the following parameters  $(d_0, z_0, \cot(\theta), \phi, \frac{q}{R})$ . Where the transverse impact parameters  $d_0$  is the signed

distanced between the origin of the coordinate frame  $r-\phi$  or x-y and the closest point on the helix (the point of closest approach). The sign of the impact parameters defines the position of the origin and the centre of the helix in the  $r-\phi$  plane. Negative corresponding to origin within helix, positive outside of helix.  $z_0$  corresponds to the z position at the point of closest approach.  $\cot(\theta)$  is the slope of the helix with respect to the z direction.  $\phi$  is the azimuthal direction of the helix at the point of closest approach.  $\frac{q}{R}$  is the charge of the particle over the helix radius, this defines the curvature and direction of the helix.

The radius of curvature is given by:

$$R = \frac{p_t}{0.3B} \quad (20)$$

Where R is in meters, transverse momentum  $p_t$  in GeV and B in tesla.

The position and momentum of a helix with starting point  $[x_s, y_s, z_s]$  and initial azimuthal direction  $\phi_s$  can be written in terms of the running parameter  $\phi$

$$x(\phi) = x_s + (\sin(\phi) - \sin(\phi_s))RQ \quad (21)$$

$$y(\phi) = y_s - (\cos(\phi) - \cos(\phi_s))RQ \quad (22)$$

$$z(\phi) = z_s + \cot(\theta)(\phi - \phi_s)RQ \quad (23)$$

$$s(\phi) = (\phi - \phi_s) \frac{R}{\sin(\theta)} \quad (24)$$

$$p_x = p \cos(\phi) \sin(\theta) \quad (25)$$

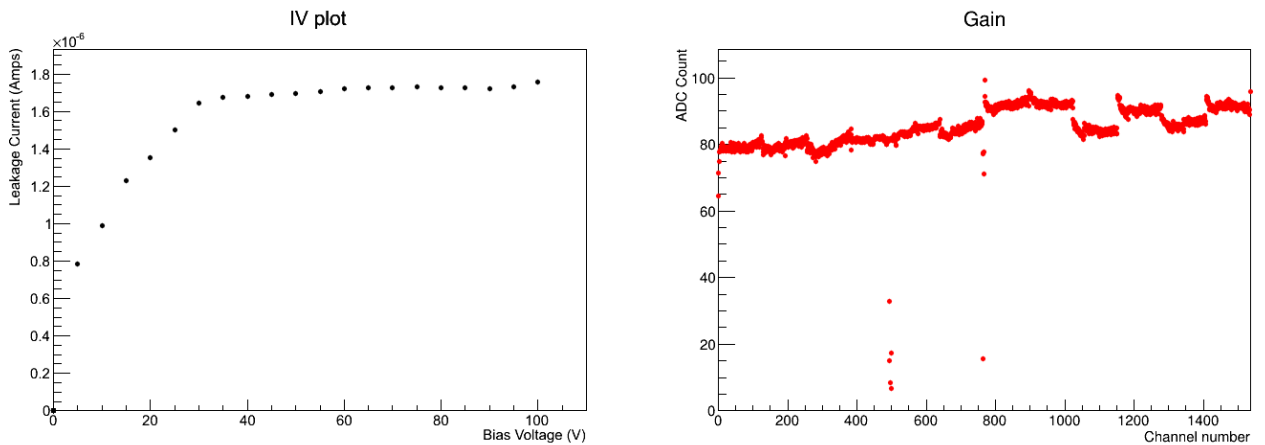
$$p_y = p \sin(\theta) \sin(\phi) \quad (26)$$

$$p_z = p \cos(\theta) \quad (27)$$

Where S is the path length of the helix.

## D Additional ladder electrical and laser results

### D.1 L3.903

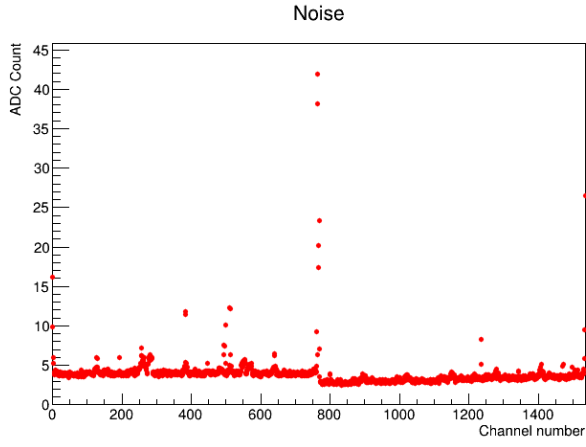


(a) Laser scan across N strips FW sub-assemblies

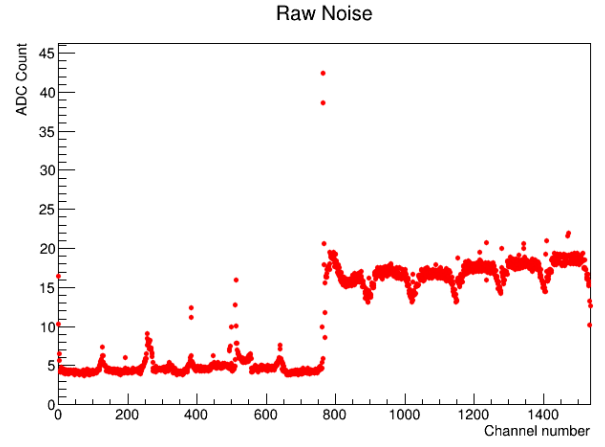
(b) Laser scan across P strips FW sub-assemblies

Figure 41: Several shorts found on the L3.903\_fw sub-assembly as seen in the gain plot



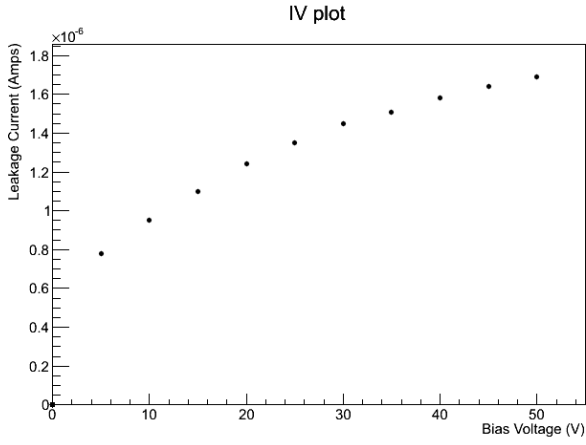


(a) Laser scan across N strips FW sub-assemblies

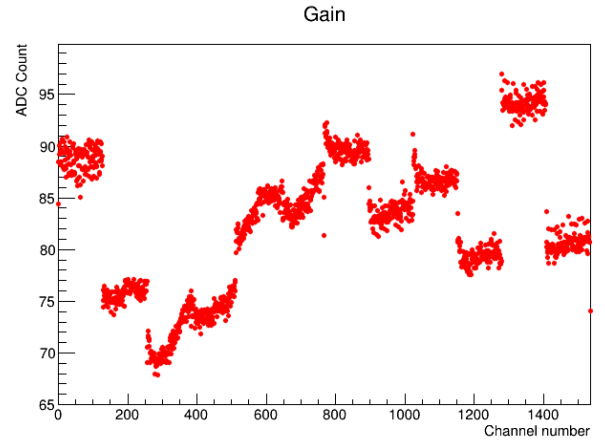


(b) Laser scan across P strips FW sub-assemblies

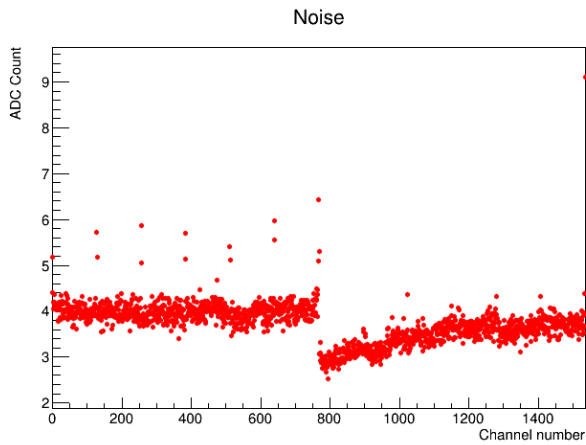
## D.2 L3.002



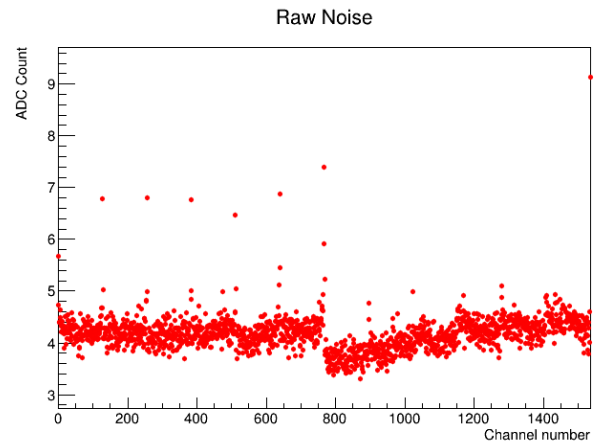
(a) L3.002\_bw IV



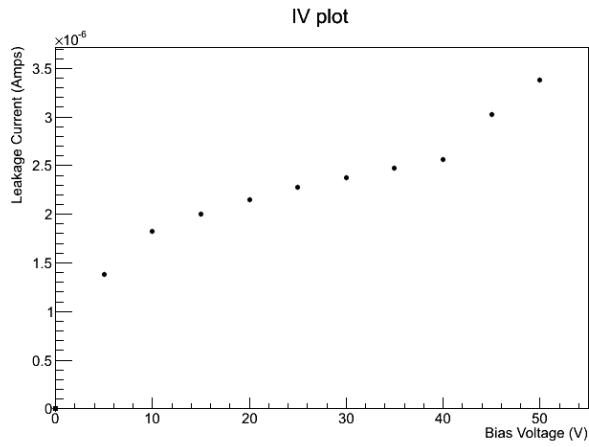
(b) L3.002\_bw gain



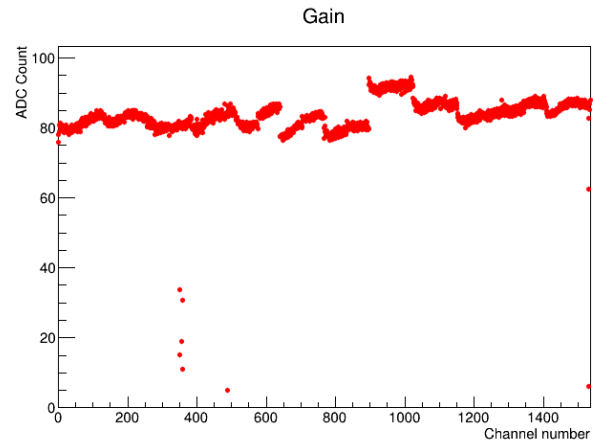
(a) L3.002\_bw noise



(b) L3.002\_bw raw noise

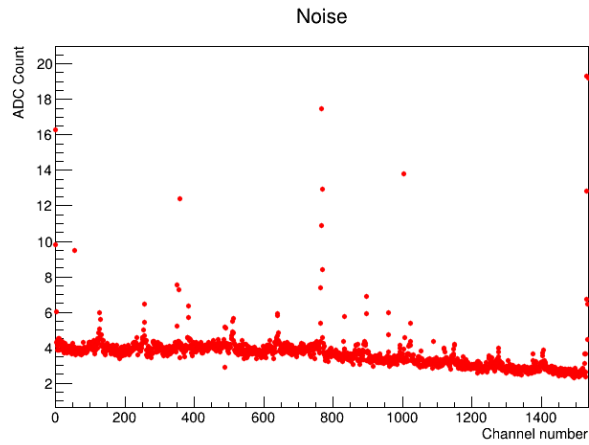


(a) L3.002\_fw IV plot. Plateau clearly at 30V, appear to pass breakdown voltage at 40V

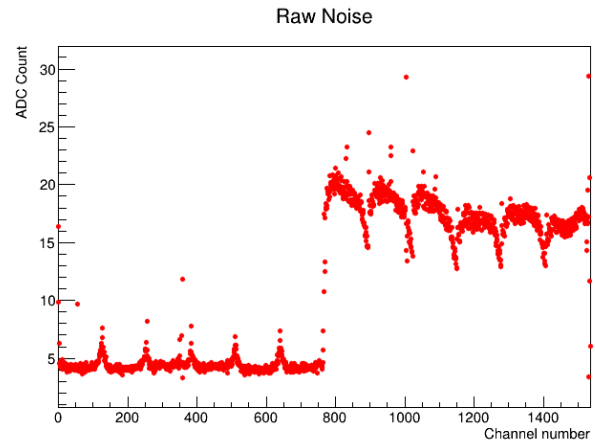


(b) L3.002\_fw gain, six channels

Figure 45: The low gain in 6 channels is evidence for 6 shorts on this sub-assembly

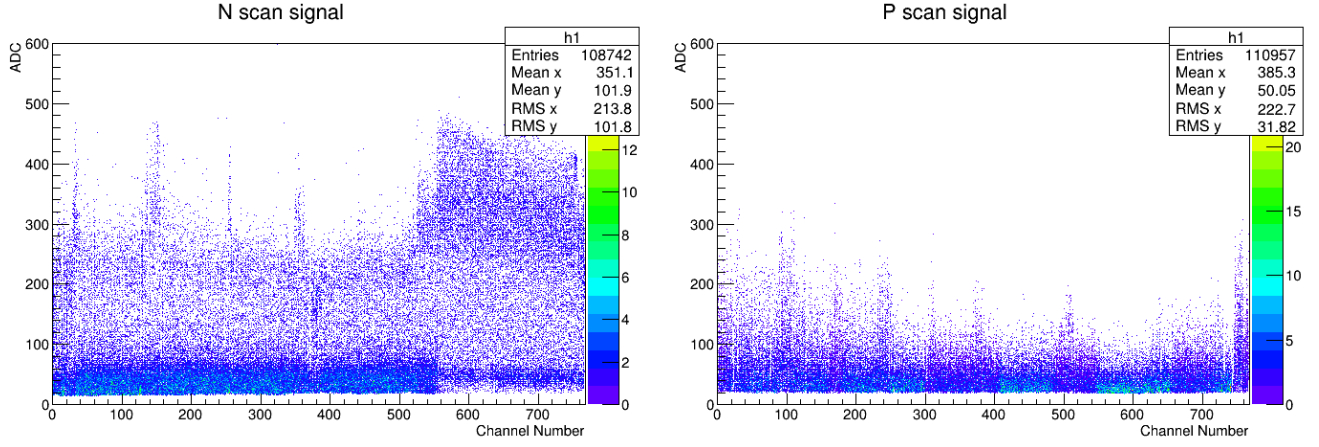


(a) Laser scan across N strips



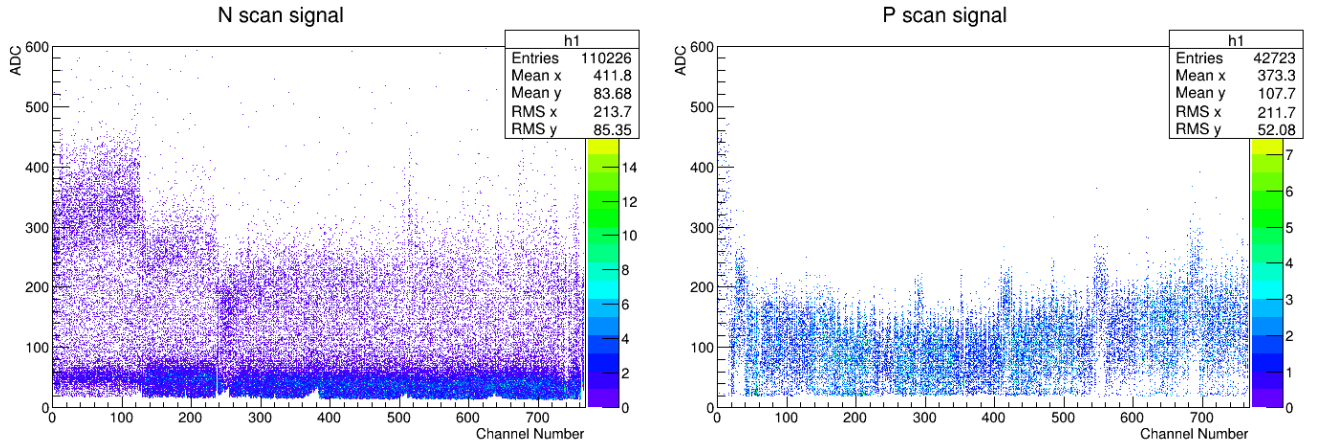
(b) Laser scan across P strips

Figure 46: The raw noise shows the higher raw noise present on the N-side of the detector prior to biasing



(a) Laser scan across N strips for BW sub-assemblies (b) Laser scan across P strips for BW sub-assemblies

Figure 47: No bad channels detected via laser scan



(a) Laser scan across N strips FW sub-assemblies

(b) Laser scan across P strips FW sub-assemblies

Figure 48: Laser scan results for P side resulted in a mistiming with the trigger, most signal is missing, the small white triangles on the N scale distribution correspond to the edge channels on the APV25 chips. It is possible for these channels to have higher noise than the other channels 46a. The high noise is cutting into the signal to noise ratio cut in place on the signal distribution.

## E Electrical Test Procedure

This procedure detailed is required by the Belle II collaborators as part of the quality control in place and is included for completeness.

- Perform initial electrical test on each of the two hybrid boards to be used in the sub-assemblies(identified as forwards, or backwards. Electrical test should include both 10k pedestal samples and calibration scan. Noise for each channel should be  $\approx 1 - 2$  ADC and gain  $\approx 90 - 100$  ADC. The gain will vary from chip to chip, but each channel on a chip should be quite consistant (to within 5 ADC). The results should be uploaded to the HEPHY database at this step, aswell as at the end of each further step in which electrical results are collected.

- Perform electrical test on hybrid sandwich ( two hybrids glued back to back). Electrical test should include both 10k pedestal samples and calibration scan. Noise for each channel should be within 20% of value recorded in individual both tests. The increase in noise is due to the electric field introduced from the additional hybrid board. The gain should remain unchanged.
- Following the wire-bonding on the P-side of the sub-assemblies, an electrical test should be performed without bias. The electrical test without bias provides limited information for the classification of open channel. The large noise of each channel resultant from the lighting of the room (turning the light closest to the sensor off provides a slight reduction of noise) and the random flow of charge carriers through the undepleted sensor, can result in good channels exhibiting similar characteristics to opens. The noise for each channel should be  $\approx 15 - 20$  ADC and gain  $\approx 40 - 50$  ADC. The main purpose of this electrical test is the identification of shorted channels. The calibration scan will reveal channels with half the gain as other channels. The efficiency of identifying shorts at this stage of assembly is quite high. All detected defects should then be confirmed under optical inspection. The distinction between shorts resulting from wire-bonds touching and shorts from scratches connecting electrodes on the sensor is not very clear and should be taken into consideration for the optical inspection.
- The above steps should be performed on the second sub-assemblies.
- The first sub-assemblies to be wire-bonded on the N-side (the backwards side) will have 192 bonds missing between the sensor and the pitch-adaptor. With this considered an electrical test should be performed, making sure to now readout both sides of the sub-assemblies. Again at this stage no bias will be applied. Results obtained at this stage will again provide the same level of information as the P-side electrical test.
- The second sub-assemblies to be wire-bonded on the N-side will have no missing bonds. No bias at this stage.
- Once the ladder is completed it can be placed inside the dark-box and one of the sub-assemblies sides can be I-V scanned. The I-V script will increment the bias voltage in steps of  $\pm 5$ V (negative to P-side, positive to N-side) every 15 seconds. The script will step the bias up to a maximum of  $\pm 50$ V. Once the script has finished there is another script to slowly step the bias voltage down.
- Following evaluation of the I-V scan, the bias voltage can be ramped up to a nominal value of  $\pm 50$ V for full depletion. An electrical test is now performed, reading out both N and P sides. Electrical test should include of 10k pedestal samples, a calibration scan and a separation voltage scan. The noise for each channel should be  $\approx 4 - 7$  ADC and gain  $\approx 70 - 80$  ADC. From this information a proper evaluation of present defects can be made. The separation voltage scan provides information for detection of pinholes. Channels with a pinhole present will exhibit an increase in ADC as the voltage is increased. The bias voltage is to be stepped down after tests have concluded.
- The ladder can now be removed from the dark-box, rotated by 180 and placed back in the dark-box so that the second sub-assemblies can be I-V scanned and electrically tested.
- Once the electrical results have been completed for both sides the output can be run through the aDefectFinder software for automatic evaluation of defects based upon user defined noise and gain selection cuts.

- A laser scan can be performed on the ladder while placed on the survey jig with the N-side facing up. In this position the laser will be in focus with the module, allow for single strip illumination. To scan the N-strips place the ladder into the dark-box parallel to the linear-stage. Make sure the laser is positioned slightly behind the first N-strip, so that the run will start with laser off the sub-assemblies. Bias the module then run the electrical testing software in hardware run. After the electrical testing has begun, run the N-side scan linear stage script. The script will move the laser across the ladder at  $160\mu\text{m/s}$ . This will result in  $\approx 100$  pulses on the laser injected into each strip. It is not possible to scan across the entire length of the sub-assemblies without going over the pitch-adaptor, the reduction in signal will need to be accounted for. After the run has ended, step down the bias voltage and removed the ladder from the dark-box. Rotated the linear-stage  $90^\circ$  and place the ladder back in the darkbox and align the P strips perpendicular to the linear-stage. Be sure the laser is slightly behind the first channel then close the dark-box and step the bias up. Begin a hardware electrical run and start the P-side scan linear stage script. The script will move the laser across the ladder at  $50\mu\text{m/s}$ .
- Repeat the laser scan for the second sub-assemblise.

## References

- [1] M. Kobayashi and T. Maskawa, “CP Violation in the Renormalizable Theory of Weak Interaction,” *Prog.Theor.Phys.* **49** (1973) 652–657.
- [2] Nobelprize.org, “The nobel prize in physics 2008.”.
- [3] **Belle-II** Collaboration, T. Kuhr, “Status of SuperKEKB and Belle II,” *PoS FPCP2010* (2010) 055, arXiv:1101.1916 [hep-ex].
- [4] **BaBar, Belle** Collaboration, A. Bevan *et al.*, “The Physics of the *B* Factories,” *Eur.Phys.J.* **C74** no. 11, (2014) 3026, arXiv:1406.6311 [hep-ex].
- [5] M. Friedl, T. Bergauer, P. Dolejschi, A. Frankenberger, I. Gfall, *et al.*, “The Belle II Silicon Vertex Detector,” *Phys.Procedia* **37** (2012) 867–873.
- [6] **Belle-II** Collaboration, T. Abe *et al.*, “Belle II Technical Design Report,” arXiv:1011.0352 [physics.ins-det].
- [7] S. Sze and K. Ng, *Physics of Semiconductor Devices*. Wiley, 2006.
- [8] V. Bartsch, W. de Boer, J. Bol, A. Dierlamm, E. Grigoriev, *et al.*, “An Algorithm for calculating the Lorentz angle in silicon detectors,” *Nucl.Instrum.Meth.* **A497** (2003) 389–396, arXiv:physics/0204078 [physics].
- [9] H. Spieler, “Semiconductor detector systems,” *Ser. Semicond. Sci. Tech.* **12** (2005) 1–489.
- [10] **Particle Data Group** Collaboration, K. Olive *et al.*, “Review of Particle Physics,” *Chin.Phys.* **C38** (2014) 090001.
- [11] B. Rossi, “High Energy Particles,”.
- [12] H. Bichsel, “Straggling in Thin Silicon Detectors,” *Rev.Mod.Phys.* **60** (1988) 663–699.
- [13] “Apvdaq reference manual.”.
- [14] C. Irmmler, *Upgrade studies for the Belle silicon vertex detector*. PhD thesis, Vienna, Tech. U., 2008.  
<http://belle.kek.jp/belle/theses/master/2008/Christianirmmler.pdf>.
- [15] M. Raymond *et al.*, “The CMS tracker APV25 0.25- $\mu$ m CMOS readout chip,” *Conf. Proc.* **C00091111** (2000) 130–134. [,130(2000)].
- [16] D. J. Lange, “The EvtGen particle decay simulation package,” *Nucl. Instrum. Meth.* **A462** (2001) 152–155.
- [17] S. D. Paganis and J.-L. Tang, “Momentum resolution improvement technique for silicon tracking detectors using dE/dx,” *Nucl. Instrum. Meth.* **A469** (2001) 311–315, arXiv:hep-ex/0104006 [hep-ex].
- [18] C. Grupen and I. Buvat, eds., *Handbook of particle detection and imaging, vol. 1 and vol.2*. Springer, Berlin, Germany, 2012. <http://www.springer.com/978-3-642-13270-4>.